1. Gutachter: Prof. Dr. Dieter Meschede
2. Gutachter: Prof. Dr. Manfred Fiebig

Contents

Chapter 1

Introduction

Quantum mechanics is one of the most important and successful theories science has ever produced. In spite of its over 100 years of success in describing various physical phenomena over a wide range of scales, there are still unresolved questions concerning the interpretational and philosophical aspects of quantum mechanics. These lead to the immense progress in experiments to confirm the theory [1]. Without being very much bothered by these and just following the "shut up and calculate!" approach, in our group, we rather concentrate ourself on exploitation of counter-intuitive quantum mechanical features of superposition and entanglement for new possible technologies, one of which for applications in quantum computing [2, 3, 4]. In quantum computing, logical information is represented by physical quantities governed by the laws of quantum mechanics. These physical quantities are two-level quantum systems called qubits (quantum bit) which can be in coherent superposition states according to the laws of quantum mechanics. A quantum computer allows several quantum algorithms which can solve certain problems much faster using qubits compared to conventional digital computers. The most popular example of these is integer factorization [5], which is hard to implement on any present or future classical computer. Several physical realizations of quantum computation have been proposed such as the ones based on ions [6], cavity QED [7], NMR [8], SQUID [9], and neutral atoms [10]. In 1996, DiVincenzo [11] has proposed five general criteria that any logical qubit candidate for a quantum computer implementation must fulfill. They are

- A scalable system with well characterized qubits.
- The ability to initialize the state of the qubits to a simple fiducial state.
- Long coherence times, much longer than the time required for logic gate operations.
- Having a universal set of quantum gates.
- A qubit-specific measurement capability.

In this introductory chapter, based on the above criteria, I briefly review the present state of the art achieved in our group towards physical realization of a quantum computer, as well the current limitations which this thesis work aims to overcome.

1.1 Quantum computing with neutral atoms

In our group we focus on coherent manipulation and control of neutral atoms which represent our qubits. One of the motivations of using neutral atoms as physical carriers of quantum information is that since they are neutral they interact very weakly with the environment, which leads to a long coherence time. The possibility to manipulate systems of neutral atoms owes to the techniques developed over the last decade for high precision spectroscopy that allow neutral atoms to be cooled to ultralow temperatures and subsequently trapped in conservative potentials. Until this time, the most promising trapping potentials for neutral atoms are optical lattices which are periodic optical potentials formed by the interference of two or more far-detuned intense laser beams. By controlling the parameters (e.g power, polarizations) of the trapping lasers, trapped atoms can be dynamically manipulated and controlled.

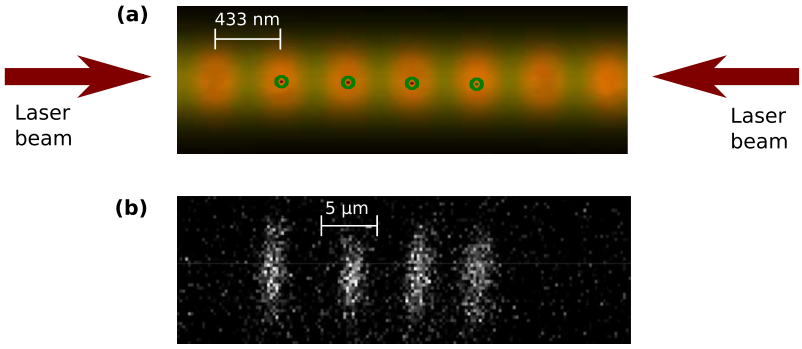

Figure 1.1: (a) Standing wave pattern formed by two counter propagating laser beams. Due to the AC Stark shift, this acts as a potential for neutral atoms. (b) Fluorescence image of atoms trapped in an optical lattice.

1.1.1 A scalable system with well characterized qubits

We use neutral Caesium (Cs) atoms as our physical carriers of quantum information. These atoms are trapped in a 1D optical lattice formed by the interference of two counter propagating linearly polarized laser beams at a wavelength of 865.9 nm, which is red detuned with respect to the D_2-transition. Due to the AC-Stark shift, the atoms are trapped in the intensity maxima of the periodic intensity pattern. A prerequisite for trapping the atoms in the optical lattice is to cool the atoms to a temperature of several milikelvin. Using the standard magneto optical trapping (MOT) technique, Cs is relatively easy to cool since the relevant transition (around 852 nm) can be addressed with commercially available diode lasers. Owing to their nuclear spin, Cs has many stable long-lived hyperfine ground states which can be used to encode our qubit states. Our qubit states are stored in the following two appropriately chosen hyperfine states

$$\begin{aligned} |0\rangle &\equiv |F = 4, m_F = 4\rangle \\ |1\rangle &\equiv |F = 3, m_F = 3\rangle . \end{aligned} \tag{1.1}$$

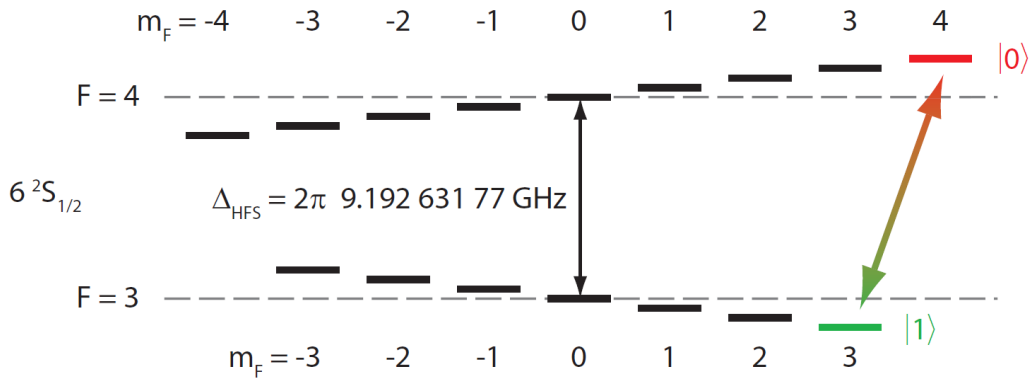

Figure 1.2: Zeeman splitting of the magnetics sublevels in the $6^2S_{1/2}$ ground state manifold of Cs. Our qubit states are stored in the outermost sublevels. Coherent transitions between the two states are driven by microwave radiation at a frequency of around 9.2 GHz.

1.1.2 The ability to initialize the state of the qubits to a simple fiducial state

When the atoms are loaded in our optical lattice from the MOT, they populate any of the magnetic sublevels of the $F = 3$ state with equal probability. In order to initialize the atoms to one of the two qubit states prior to further manipulation, an optical pumping technique is employed. Our atoms are initialized to the state $|0\rangle$ by illuminating them with a σ^+-polarized laser beam which is resonant to the $F = 4 \rightarrow F' = 4$ transition. At the same time, a laser beam resonant to the $F = 3 \rightarrow F' = 4$ is applied to bring the atoms to the pumping cycle. A weak magnetic field of 3 G is applied along the beam axis to define the quantization axis. Due to the selection rules, the atoms can only undergo transitions to the excited states $F' = 4$ with higher magnetic sublevels and decay back to the ground states. After several transitions, all atoms occupy the state $|0\rangle$ which cannot undergo further transitions and just stay in the so-called dark state.

Coherent transitions between the states $|0\rangle$ and $|1\rangle$ are then driven by microwave radiation at a frequency of around 9.2 GHz. The corresponding Rabi frequency is given by

$$\Omega_{\mathrm{MW}} = -\frac{\hat{\mathbf{d}} \cdot \mathbf{B}_{\mathrm{MW}}}{\hbar} \tag{1.2}$$

where $\hat{\mathbf{d}}$ is the magnetic induced dipole moment of the atom and $\mathbf{B}_{\mathrm{MW}}$ denotes the magnetic field vector. To prepare the atoms in the state $|1\rangle$, a π-pulse, which satisfies the condition

$$\int_0^\tau \Omega_{\mathrm{MW}}(t)dt = \pi\,, \tag{1.3}$$

is applied to the atoms. Here τ is the irradiation time. Analogously, to prepare the atoms in a balanced superposition state $|\Psi\rangle = \frac{1}{\sqrt{2}}(|0\rangle) + i\,|1\rangle$, a $\frac{\pi}{2}$-pulse is applied.

1.1.3 Long coherence times, much longer than the time required for logic gate operations

The coupling of the system with its enviroment leads to decoherence. As a consequence, qubit information that has been stored would be lost. Owing to their neutrality, neutral

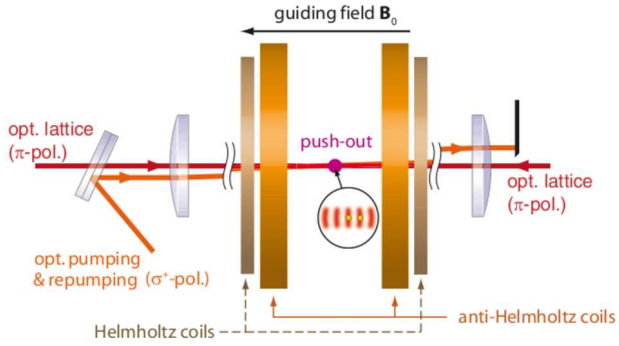

Figure 1.3: Schematic of the setup of our optical lattice and optical pumping system.

atoms are relatively weakly coupled to the environment, thus reducing decoherence. This serves as one of the advantages of neutral atoms over other candidates for physical implementations of qubits. The time characterizing the timescale on which the stored qubit information is preserved is refered to as coherence time. It can be classified into two catogaries: longitudinal coherence time, T_l and transversal coherence time, T_t.

T_l describes the decay of the population of the qubit states. In our system, the main mechanism that leads to the decay is the scattering of photons from the laser of the dipole trap in which our atoms are trapped. In the current situation, the photon scattering rate in our system is of the order of 100 photons per second, equivalent to a coherence time of 10 ms. It is considerably long for our qubit operations and plays a minor role.

T_t on the other hand, describes the more dominant decoherence mechanism caused by technical imperfections of the experimental setup, for examples, fluctuations in the power of the dipole trap lasers and in the strength of the magnetic field defining the quantization axis.

1.1.4 Having a universal set of quantum gates

Any operation on a register of qubits can be constructed from a combination of one-bit gates and two-bit gates [12]. An example of a two-bit gate is the "controlled-NOT" (CNOT) gate which is based on entangled states.

The task of entangling neutral atoms is quite challenging since they interact weakly with each other. In 1999, a physical realization for entangling neutral atoms in optical lattices by means of cold controlled collisions has been proposed [13]. In the proposed scheme, two atoms in neighbouring lattice sites, each in a superposition of their internal states, are split to the right and to the left depending on the state until the wavepackets of different states are brought into a single lattice site and interact with each other (see Fig.1.4). Due to elastic collision the atoms acquire some collisional phase φ_int depending on the interaction time τ:

$$\begin{aligned}\varphi_{\text{int}} &= \frac{1}{\hbar}\int_0^\tau dt \Delta E(t) \\ \Delta E(t) &= \frac{4\pi a_s \hbar^2}{m}\int dx |\psi_{|1\rangle}(x,t)|^2 |\psi_{|0\rangle}(x,t)|^2\end{aligned} \tag{1.4}$$

where a_s denotes the s-wave scattering length between the states $|0\rangle$ and $|1\rangle$, $\psi_{|i\rangle}$ is the wavepackets of the state $|i\rangle$, and m the mass of Cs. The wavepackets are then brought back to the initial position by reversing the potential shift. The transformation of the states after a complete sequence has the following form

$$\begin{aligned}|0\rangle \otimes |0\rangle &\rightarrow |0\rangle \otimes |0\rangle \\ |0\rangle \otimes |1\rangle &\rightarrow |0\rangle \otimes |0\rangle \\ |1\rangle \otimes |0\rangle &\rightarrow |1\rangle \otimes |0\rangle \cdot e^{i\varphi_{\text{int}}} \\ |1\rangle \otimes |1\rangle &\rightarrow |1\rangle \otimes |1\rangle .\end{aligned} \tag{1.5}$$

If the duration of the interaction time is chosen carefully and by combining with two additional 1-qubit gates, a CNOT gate can be constructed [14].

Experimentally, this scheme can be accomplished with the aid of a so-called state dependent lattice potential, in which atoms are state-selectively trapped and transported. In the last decade, state-selective transport of Bose-Einstein condensates of Rubidium atoms has been realized [15], demonstrating entanglement via controlled cold collisions [16].

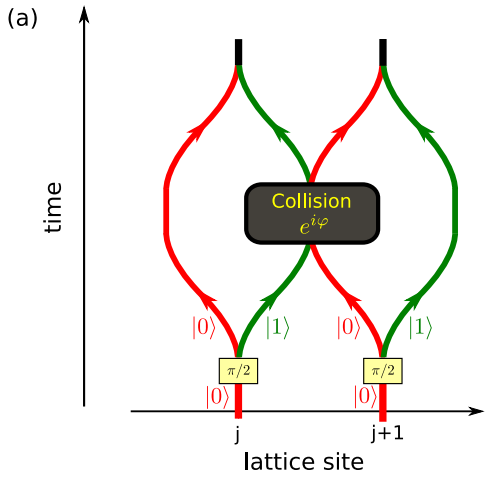

Figure 1.4: Scheme for creating entangled states of atoms. Two atoms in the initial state $|0\rangle$ in neighbouring lattice sites are prepared in a superposition of their internal states by applying a microwave $\frac{\pi}{2}$-pulse. Subsequently, the two states are split to the left and to the right by displacing the potentials until the wavepackets of differet states occupy the same lattice site and interact with each other. After some interaction time, the atoms are brought back to the initial position by reversing the displacement.

State dependent lattice

In our case, a state dependent optical lattice can be realized by tuning the linearly polarized optical lattice laser between the D_1- and D_2-transitions of the Cs atom. As a result, for an atom in the state $|J = \frac{1}{2}, m_J = -\frac{1}{2}\rangle$, the σ^+-component of the laser is red and blue detuned with respect to the D_1- and D_2-transitions, respectively, whereas the σ^--component is only red detuned (see Fig. 1.5). There exists a certain wavelength, called the magic wavelength λ_m, at which the contributions from the σ^+-component cancel out and the atom only experiences an attractive contribution from the σ^--component. By the same token the state $|J = \frac{1}{2}, m_J = \frac{1}{2}\rangle$ experiences the same effect but with the opposite light polarization.

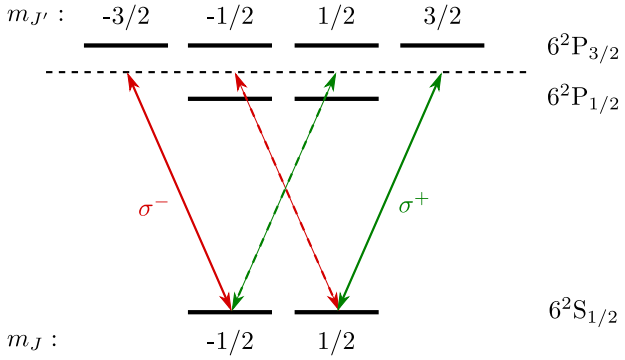

Figure 1.5: Zeeman sublevels of the ground state and the first two excited states of cesium under neglect of the influence of the nucleus spin. At the magic wavelength λ_m, each of the ground state sublevels experiences only the contribution from one of the circularly polarized components which is indicated by the solid line.

With the help of the Clebsch Gordon coefficients, the states $|0\rangle$ and $|1\rangle$ can be decomposed in terms of the basis of the nuclear spin I and electronic spin J:

$$\begin{aligned} |0\rangle \equiv |F = 3, m_F = 3\rangle = &\sqrt{\frac{1}{8}}|I = \frac{7}{2}, m_I = -\frac{5}{2}\rangle \otimes |J = \frac{1}{2}, m_J = -\frac{1}{2}\rangle \\ &+ \sqrt{\frac{7}{8}}|I = \frac{7}{2}, m_I = -\frac{7}{2}\rangle \otimes |J = \frac{1}{2}, m_J = +\frac{1}{2}\rangle \\ |1\rangle \equiv |F = 4, m_F = 4\rangle = &\quad |I = \frac{7}{2}, m_I = -\frac{7}{2}\rangle \otimes |J = \frac{1}{2}, m_J = -\frac{1}{2}\rangle. \end{aligned} \tag{1.6}$$

From this relation, we infer that the state $|1\rangle$ consists of only one fine structure state ($|J = \frac{1}{2}, m_J = -\frac{1}{2}\rangle$) which is only coupled to σ^--polarized light, whereas the state $|0\rangle$ is coupled to both polarizations with dominant contribution from σ^+-polarized light. Thus, by using a linearly polarized standing wave light at the wavelength λ_M, which can be decomposed into σ^+ and σ^--polarized light, each qubit state is coupled almost exclusively to one of the two circularly polarized light. The two confining potentials can be moved in the opposite directions relative to each other by changing the relative polarization angle between the two linearly polarized counterpropagating laser beams forming the optical lattice. In our setup, an Electro-Optical Modulator (EOM), in combination with a fixed $\lambda/4$ wave-plate is used to precisely control the relative polarization angle [17].

Eventhough we are already equipped with a state dependent lattice, creation of entangled states as described previously has not been demonstrated in our group. This owes to the fact

that in order to perform such cold controlled collisions, it is mandatory to have the atoms occupying the motional ground state of the trapping potential in all 3 dimensions. Different from experiments with Bose-Einstein condensates loaded in optical lattices in which atoms are already in the ground state of the trapping potentials [18], in our experiment we load our lattice with laser cooled atomic gases with a temperature of around 10 μK. The atoms occupy various vibrational states after the loading process. Further cooling technique which is a resolved sideband cooling is required to cool the atoms to the ground state. Since the difference between the frequency spacings in the axial and the radial direction is very large, sideband cooling in both directions need to be performed seperately. We have demonstrated ground state cooling of the atoms along the axial direction but not along the radial direction due to some constraints as described below.

Axial ground state cooling

We have demonstrated a novel technique to sideband cool the atoms to the ground state by utilizing our state dependent optical lattice and microwave radiation [19]. In the typical sideband cooling technique based on lasers, arbitrary pairs of vibrational states are coupled via the recoil of the laser photons. This is not true in case of microwaves since thier photons have a negligible recoil. Nevertheless, in our state dependent optical lattice, microwave radiation can still drive transitions between any pairs of vibrational states, whose wavefunctions are controllably overlapped by state-selectively displacing the $|0\rangle$ and $|1\rangle$ states by a distance Δx. By tuning the microwave frequency to the sideband that lower the vibrational quantum number, we are able to cool the atoms to the ground state with a population of 97%.

Radial sideband cooling

The same microwave cooling technique is not applicable for motional ground state cooling along the radial direction because along this direction the potentials for the two internal atomic states cannot be spatially displaced with respect to each other. The most commonly used scheme for motional ground state cooling is resolved Raman sideband cooling which is a laser driven scheme [21]. In Fig. 1.6, this scheme is summarized.
In this process, the atom will inevitably acquire a recoil energy, $\epsilon_{\mathrm{rec}} = \hbar\nu_{\mathrm{rec}}$ from each spontaneously emitted photon of frequency ν_{rec}. This could result in excitation of a vibrational quantum which will prevent the atom from ending up in the ground state $|g, 0\rangle$. To avoid this, the energy spacing between vibrational levels needs to be large enough so that the recoil energy provided by the emitted photons is not sufficient to excite a vibrational quantum. This is possible in the so-called Lamb-Dicke regime in which the condition $\eta^2 = \frac{\epsilon_{\mathrm{rec}}}{\hbar\Omega} \ll 1$ is satisfied, where η is known as the Lamb-Dicke parameter.

Currently, our atoms are confined radially by the Gaussian profile of the lattice beams. With typical parameters of 120 mW optical power and 20 μm waist radius, it provides a weak confinement with a trapping frequency of $2\pi\times1.1$ kHz, much weaker compared to that along the axial confinement. The situation can already be seen from Fig. 1.1(b), where one can think of the sites of the lattice as having a pancake-like shape. The Lamb Dicke parameter in this case is equal to 0.97, which is not small enough to permit any ground state cooling scheme to be carried out [20].

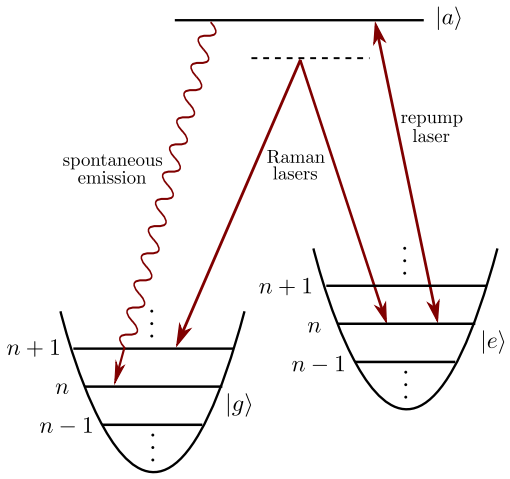

Figure 1.6: Schematic illustration of resolved Raman sideband cooling technique. A pair of Raman lasers off-resonant from a transition to an auxiliary state $|a\rangle$ drives a dipole forbidden transition between two internal atomic states $|g\rangle$ and $|e\rangle$. The frequency difference between these two lasers is chosen to resonantly couple $|g, n\rangle$ and $|e, n-1\rangle$. In this way, one motional quantum number is removed for each transition. To close the cooling cycle via a spontaneous emission process, a third laser field, the repump laser, which is resonant with the $|e\rangle$ to $|a\rangle$ transition is employed. Over several of this absorption emission events, the atom ends up in the ground state $|g, 0\rangle$ which is dark to the laser fields.

1.2 This thesis

In order to overcome the current limitions described above, the energy spacing in the radial direction needs to be increased by having a tighter confinement. This can be accomplished by introducing an additional blue-detuned laser beam with a dark region in the center, overlapped with the exiting standing wave optical lattice. In addition to increasing the energy spacing, the tighter confinement provided by such a laser beam would also benefit the demonstration of controlled cold collisions since a tighter confinement implies smaller wavepacket spreads. Refering to Eq (1.4), this means that the ovelap integral of the wavepackets can be increased, which shortens the interaction time required for atoms to acquire the desired collisional phase.

In Chapter 2, several methods to generate a laser beam with a center dark region is discussed. The most appropiate one for our purpose is chosen and discussed in more detail.

The dipole potential for Cs atoms formed by the laser beam is evaluated in Chapter 3. The trapping frequency of the potential as a function of the laser parameters is estimated. The photon scattering rate in the potential is calculated. This will exhibits one of the advantages of using the laser beam to trap atoms.

In Chapter 4, the experimental setup towards integrating the generated laser beam into the main experiment is proposed and discussed.

Chapter 2

Laser beam with a center dark region

A laser beam with a dark region in the center (which is from now on called a donut beam) arises whenever the beam posseses an azimuthal phase structure $\exp(il\phi)$. The presence of this azimuthal phase indicates that the phase of the beam changes continuously from 0 to $2l\pi$ with a round trip on any circle around the center in the (ρ, ϕ)-plane. The integer l is called the topological charge. Thus, for every source point (ρ, ϕ) there is an accompanying source point $(\rho, \phi+\pi/l)$ and they interfere destructively along the beam axis. This gives rise to a dark region in the center of the beam. Examples of such beams are Laguerre-Gaussian beams and high-order Bessel beams.

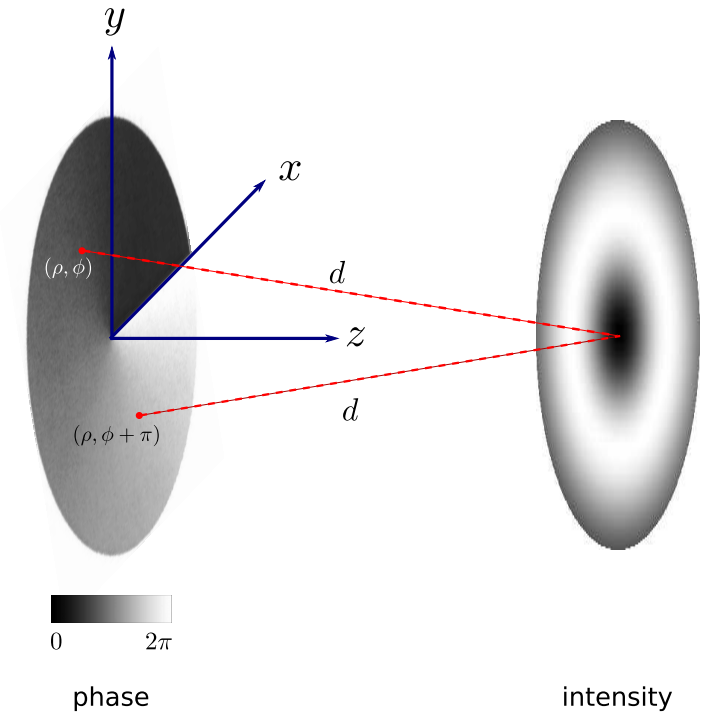

Figure 2.1: Phase distribution corresponding to the multiplier $\exp(il\phi)$ with $l = 1$, and the corresponding intensity profile of a donut beam.

2.1 Generation of a donut beam

There exist several experimentally proven methods to produce a donut beam:

- Mode-conversion
- Computer-generated hologram
- Spiral phase plate

I have investigated these methods in detail and choose the most practical one for our purpose.

2.1.1 Mode-conversion

Laguerre-Gaussian (LG) modes form a complete set of solutions of the wave equation in cylindrical coordinates. Their field amplitudes are given by [24]

$$\begin{aligned} u_{p,l}^{\mathrm{LG}}(r,\phi,z) =& \frac{C_{pl}^{\mathrm{LG}}}{(1+z^2/z_R^2)^{1/2}} \left[\frac{r\sqrt{2}}{w(z)}\right]^l L_p^l \left[\frac{2r^2}{w^2(z)}\right] \exp\left[-\frac{r^2}{w^2(z)}\right] \\ & \times \exp\left[\frac{ikr^2 z}{2(z^2+z_R^2)}\right] \exp(il\phi) \exp\left[i(2p+l+1)\arctan\left(\frac{z}{z_R}\right)\right], \end{aligned} \tag{2.1}$$

where L_p^l denotes the associated Laguerre polynomial, C_{pl}^{LG} is a normalization factor and the integers variables p and l represent the radial and azimuthal mode indices, respectively. The presence of the factor $\exp(il\phi)$ implies that LG modes have a center dark region. The LG modes can be written as a superposition of another set of solutions of the wave equation which is Hermite-Gaussian modes

$$\begin{aligned} u_{n,m}^{\mathrm{HG}}(x,y,z) =& \frac{C_{nm}^{\mathrm{HG}}}{w(z)} \exp\left(-ik\frac{(x^2+y^2)^2}{2(z^2+z_R^2)}\right) \exp\left(-\frac{x^2+y^2}{w^2(z)}\right) \\ & \times \exp\left[-(n+m+1)\arctan\left(\frac{y}{x}\right)\right] H_n\left(\frac{\sqrt{2}x}{w(z)}\right) H_n\left(\frac{\sqrt{2}y}{w(z)}\right), \end{aligned} \tag{2.2}$$

where $H_n(x)$ and $H_m(y)$ are Hermite polynomial of orders n and m, respectively. The transformation from LG modes to HG modes reads [28]

$$u^{\mathrm{LG}_{p,l}}(\rho,\phi,z) = \sum_{k=0}^{m+n} i^k b(,m,k) u_{m+n-k,k}^{\mathrm{HG}}(x,y,z), \tag{2.3}$$

with the transformation coefficient

$$b(n,m,k) = \sqrt{\frac{(n+m)!k!}{2^{n+m}n!m!}} \times \frac{1}{k!}\frac{d^k}{dt^k}[(1-t)^n(1+t)^m]_{t=0}. \tag{2.4}$$

For example the LG_{01} mode can be written as a superposition of the HG_{01} and the HG_{10} modes with a phase difference of $\pi/2$:

$$u_{0,1}^{\mathrm{LG}}(\rho,\phi,z) = \frac{1}{\sqrt{2}}\left(u_{1,0}^{\mathrm{HG}}(x,y,z) + iu_{0,1}^{\mathrm{HG}}(x,y,z)\right). \tag{2.5}$$

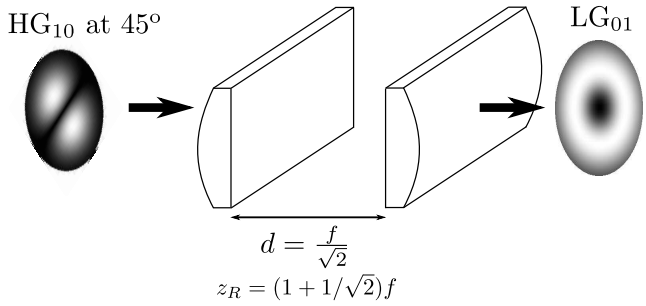

Figure 2.2: Cylindrical lens mode converter used to transfrom HG modes into LG modes.

Experimentally the mode-conversion of Eq. (2.5) can be accomplished by using a combination of two cylindrical lenses with a HG_{10} mode, oriented at 45° with respect to the cylindrical axis of the lens, as the input [25]. This HG_{10} mode at 45° can be written as a superposition of the HG_{10} and HG_{01} modes which are in phase. The role of the cylindrical lenses is to exploit the Gouy phases of the two modes such that the difference between them is equal to $\pi/2$. This can be achieved if the following conditions are satisfied [28]

$$\begin{aligned} d &= \frac{f}{\sqrt{2}} \\ z &= (1 + \frac{1}{\sqrt{2}})f \end{aligned} \tag{2.6}$$

Here d is the separation between the two lenses of focal length f and z_R denotes the Rayleigh range of the incident beam. The complexity of this method is that the input beam in not the fundamental mode but instead the HG_{10} mode which is not that easy to produce with high efficiency.

2.1.2 Computer-generated hologram

A hologram is essentially a record of the interference pattern of two fields, a reference field and an object field, which are coherent. Typically this is done by splitting a laser beam to obtain the two coherent beams. One is used as a reference field and the other one is reflected from the object of interest. The two are then interfered and recorded on a recording plate.

Since producing a hologram requires only the superposition of the reference field and the object fields, it is possible to calculate the resulting interference pattern using a computer. Such a hologram is usually called a computer-generated hologram (CGH). It has been shown in several papers how CGHs can be designed [26, 27]. In our case, the field of interest is the one that carries an azimuthal phase factor, $E_{\text{obj}} = e^{il\phi}$. When interfered with a reference plane wave $E_{\text{ref}} = e^{ik_z z}$ tilted at an angle $\theta = k_z/k$, the resulting interference pattern has the form

$$H = |\psi_{\text{obj}} + \psi_{\text{ref}}|^2 = |e^{i\phi} + e^{ik_z z}|^2 = 2[1 + \cos(k_z z - l\phi)] \tag{2.7}$$

The holographic pattern H for topological charge $l = 1$ is shown in Fig. 2.3. When illuminated with a Gaussian beam, the output consists of several beams with different diffraction orders. A donut beam with topological charge $\pm l$ can be obtained from the ± 1-st order diffracted beam.

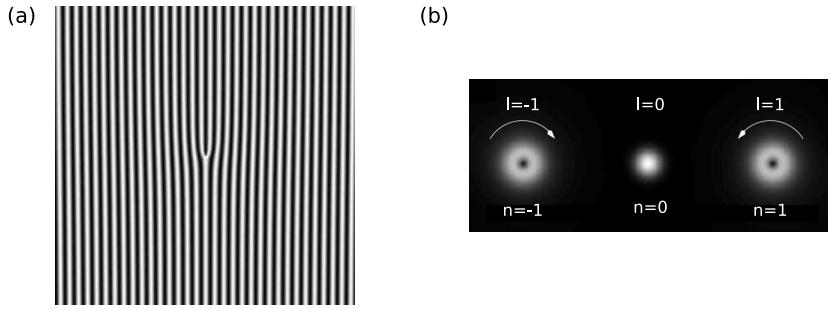

Figure 2.3: (a) Computer generated hologram for producing donut beams with topological $l = \pm 1$. (b) By illuminating this hologram with a Gaussian beam, a donut beam with topological charge $l = \pm 1$ is produced in the ± 1 diffraction order.

A disadvantage of employing this method of creation is that, since it relies on a diffracted beam, the highest efficiency one would expect is around 70 - 80%. Nevertheless, a donut beam with topological charge l is known to carry orbital angular momentum equal to $l\hbar$ [24]. Owing to its flexibility in generating donut beams of various topological charges, this method might be useful for generating a donut beam which can be used as an auxiliary laser field which can manipulate the orbital angular momentum of an atom trapped in a conservative potential [29].

2.1.3 Spiral phase plate

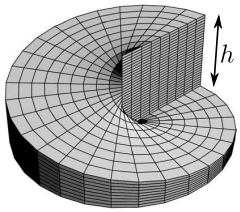

Figure 2.4: Spiral phase plate. The thickness of the plate increases proportional to the azimuthal angle.

A more straightforward way of imprinting a phase factor $\exp(il\phi)$ into any beam is by employing a phase plate that has an increasing thickness proportional to the azimuthal angle. Since the phase of the light leaving the plate is directly proportional to the length of the time it takes for the light to pass through it, this so-called spiral phase plate (SPP) introduces a phase factor, that is a function of the azimuthal angle $\exp(il\phi)$, to any beam incident on it. The topological charge is determined by the following expression [28]

$$l = \frac{\Delta n \cdot h}{\lambda}. \tag{2.8}$$

Here h is the step height, Δn denotes the difference of refractive index between the SPP and its surrounding and λ is the wavelength of the incident beam. Commercial SPP's (RPC photonic), made of polymer replicated on a glass substrate, have a sufficiently high damage threshold (> 1W). It also converts nearly 100% of the incident beam into a donut beam. Based on these robutness, this method of creation will be employed in pursuing the goal of

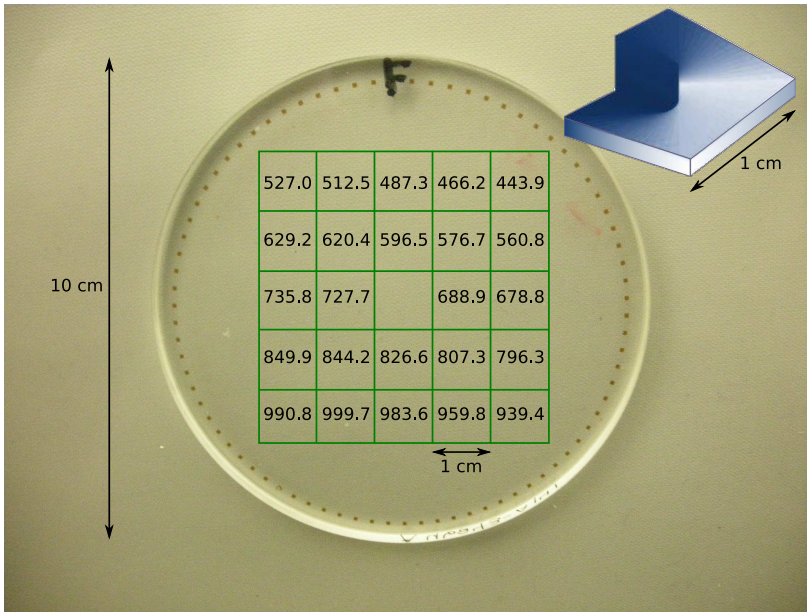

Figure 2.5: SPP's by RPC photonics. The 24 SPP's with various step heights are replicated on a glass substrate. Each SPP is hardly seen by eyes. The upper right picture is a cartoon illustration of each SPP.

this project. The rest of this chapter will mainly concentrate on a donut beam created by a SPP manufactured by the company RPC photonic.

The commercial SPP's from the company RPC photonics are produced using lithographic techniques. There are 24 of them with various step heights replicated on the same glass substrate. According to the manufacturer's specification, the SPP's introduce a phase factor $\exp(i\phi)$ (topological charge $l = 1$) to an incident beam with various wavelengths, as shown in Fig. 2.5. The most relevant one for this project is that for a wavelength of 849.9 nm. This wavelength will be denoted by λ_1. A donut beam generated by the SPP is discussed in detail in the following.

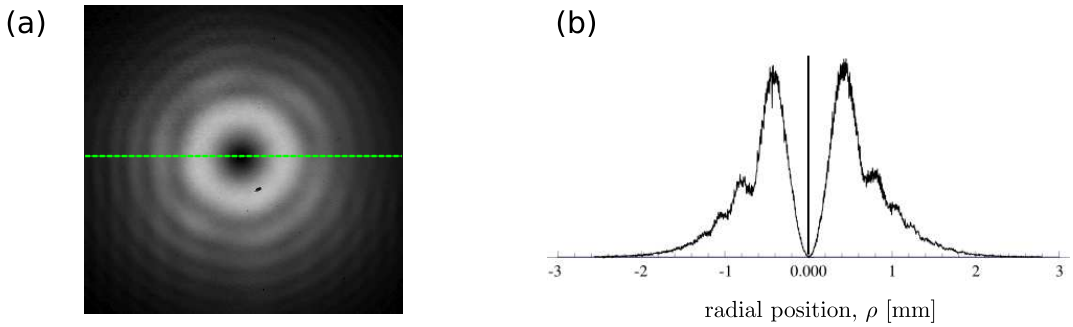

Figure 2.6: (a) Beam profile image of a donut beam generated by the SPP. (b) One dimensional radial intensity distribution of the donut beam taken along a straight line passing through the beam center (green line in (a)).

2.2 Donut beam generated by the SPP

A donut beam generated by the SPP is shown in Fig. 2.6. The experimental setup to generate the donut beam is discussed in Sec. 2.2.2. To be able to carry out later analysis of atoms trapped in the donut beam, it is necessary to obtain a mathematical expression that describes its intensity distribution.

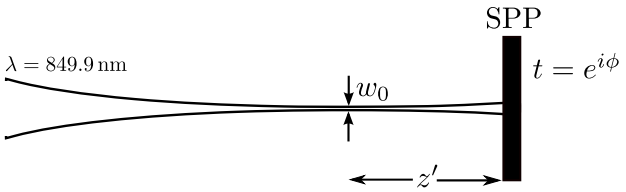

Figure 2.7: Spiral phase plate illuminated by a Gaussian beam at position z' from the position of the beam waist.

Let us consider the SPP illuminated with a Gaussian beam with wavelength λ_1

$$E(\rho,\phi,z) = E_0 \frac{w_0}{w(z)} \exp\left(\frac{-\rho^2}{w^2(z)}\right) \exp\left(-ikz - ik\frac{r^2}{2R(z)} + i\zeta(z)\right), \tag{2.9}$$

where

$$\begin{aligned}
k &= \frac{2\pi}{\lambda_1}, \qquad \text{wave number} \\
w(z) &= w_0\sqrt{1+\left(\frac{z}{z_R}\right)^2}, \qquad \frac{1}{e^2} - \text{beam radius} \\
R(z) &= z\left(1+\left(\frac{z_R}{z}\right)^2\right), \qquad \text{curvature radius of the wavefront} \\
\zeta(z) &= \tan^{-1}\left(\frac{z}{z_R}\right), \qquad \text{Gouy phase} \\
z_R &= \frac{\pi w_0^2}{\lambda_1}, \qquad \text{Rayleigh range,} \\
E_0 &= \sqrt{\frac{2P}{\pi w_0^2}}, \qquad \text{and} \\
P, &\qquad \text{power.}
\end{aligned} \tag{2.10}$$

Assuming the beam hits exactly at the center of the SPP, immediately behind the spiral phase plate, the field amplitude takes the form

$$E(\rho',\phi',z') = E_0 \frac{w_0}{w(z')} \exp\left(\frac{-\rho'^2}{w^2(z')}\right) \exp\left(-ikz' - ik\frac{\rho'^2}{2R(z')} + i\zeta(z')\right) \exp(i\phi'), \tag{2.11}$$

where we assume that the SPP is illuminated at position z' from the position of the beam waist (see Fig. 2.7). Eq. (2.11) is our intial field which we want to propate to any later point (ρ,ϕ,z) behind the SPP. This can be done with the help of scalar diffraction theory.

2.2.1 Scalar diffraction theory

According to the Huygens-Fresnel principle every point on the wavefront of a disturbance acts as a secondary point source whose wavelet then mutually interferes with each other to form the wavefront at a later instant, as illustrated in Fig. 2.8. This principle was summarized into a mathematical foundation by Gustav Kirchhoff which is then known as Kirchhoff's diffraction theory [30]:

$$E(x,y,z) = -\frac{iA}{2\lambda}\iint_{\mathcal{A}} \frac{e^{ik(r+s)}}{rs}[\cos(n,r) - \cos(n,s)]dS \tag{2.12}$$

It allows one to calculate the field distribution of a light emerging from a diffracting object as well as to propagate a known field amplitude at an initial point (x_0, y_0, z_0) to any desired observation point (x, y, z). From Eq. (2.12), with appropriate approximations, several simplified diffraction integrals can derived such as the Fresnel integral

$$E(x,y,z) = -\frac{i}{\lambda z}e^{ikz}\iint E(x_0,y_0,z_0)e^{\frac{ik}{2z}[(x-x_0)^2+(y-y_0)^2]}dx_0dy_0 \tag{2.13}$$

which can be used to propagate an initial field amplitude at point (x_0, y_0, z_0) to a final point (x, y, z) through free space.

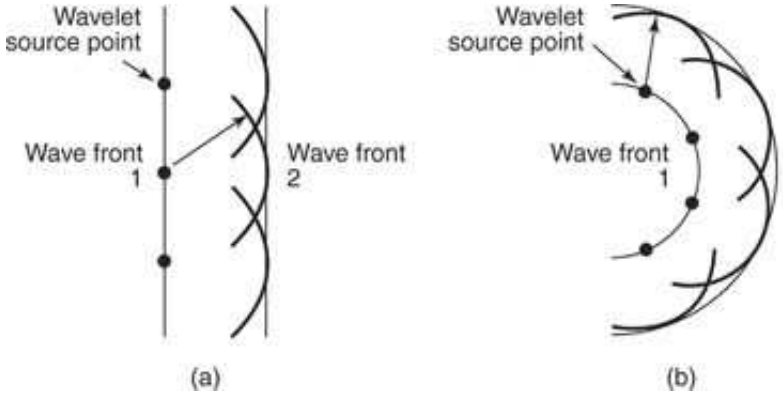

Figure 2.8: Huygens-Fresnel principle. Every point on the wavefront of a disturbance acts as a secondary point source whose wavelet then mutually interferes with each other to form the wavefront at a later instant.

In most experiments it is necessary to focus, modify, or shape the laser beam using lenses and other optical elements. In the paraxial approximation, the effects of these optical elements on paraxial beams are best described by 2×2 matrices known as the ray transfer matrices. The ray transfer matrices for some optical elements which are relevant to us are given in Table 2.1. For an optical system consisting of n elements, whose ray transfer matrices are $\mathbf{M}_1, \mathbf{M}_2, ..., \mathbf{M}_n$, the total ray transfer matrix of the system, $\mathbf{M}_{\text{tot}}$ can be obtained by taking the matrix multiplication of the ray transfer matrices of the individual optical elements

$$\rightarrow \boxed{\mathbf{M}_1} \rightarrow \boxed{\mathbf{M}_2} \rightarrow \cdots \rightarrow \boxed{\mathbf{M}_n} \rightarrow \qquad \mathbf{M}_{\text{tot}} = \mathbf{M}_n \cdot \cdots \cdot \mathbf{M_2} \cdot \mathbf{M_1}\,. \tag{2.14}$$

Let us now consider the propagation of a beam through an optical system of total ray transfer matrix $\mathbf{M}_{\text{tot}} = \begin{pmatrix} A & B \\ C & D \end{pmatrix}$. We would like to know the field distribution after the

Element	Matrix
Free space propagation	$\begin{pmatrix} 1 & d \\ 0 & 1 \end{pmatrix}$
Reflection from a flat mirror	$\begin{pmatrix} 1 & 0 \\ 0 & 1 \end{pmatrix}$
Thin lens with focal length f	$\begin{pmatrix} 1 & 0 \\ -1/f & 1 \end{pmatrix}$
Telescope with magnification $\mathcal{M} = -\frac{f_2}{f_1}$	$\begin{pmatrix} \mathcal{M} & f_1 + f_2 \\ 0 & 1/\mathcal{M} \end{pmatrix}$

Table 2.1: Some important $ABCD$ matrices [31].

optical system from the knowledge of the intial field distribution before the optical system, i.e., we want to propagate any initial field amplitude through the optical system. This can be accomplished with aid of the Collins integral [32]

$$\begin{aligned} E(x,y,z) = &- \frac{i}{\lambda B} e^{ikz} \\ &\times \iint E_0(x',y',z') e^{i\frac{\pi}{\lambda B}[A(x'^2+y'^2)+D(x^2+y^2)-2(x'x+y'y)]} dx'dy' \end{aligned} \tag{2.15}$$

which is a generalized Kirchhoff integral written in terms of the elements of the total ray transfer matrix of the system. Note that for a system that consists of just free space, whose ray transfer matrix is given by $\begin{pmatrix} 1 & z \\ 0 & 1 \end{pmatrix}$, the Collins integral just becomes the Fresnel integral (Eq. (2.13)). In polar cylindrical coordinates, the Collins integral takes the form

$$\begin{aligned} E(\rho,\phi,z) = &- \frac{i}{\lambda B} e^{ikz} \\ &\times \int_0^\infty E(\rho',\phi',z') \exp\left[\frac{ik}{2B}(A\rho'^2 + D\rho^2)\right] \\ &\times \int_0^{2\pi} \exp\left[\frac{-ik\rho\rho'\cos(\phi-\phi')}{B}\right] \rho' d\rho' d\phi'. \end{aligned} \tag{2.16}$$

2.2.2 Propagation of the donut beam through optical components

To see the propagation of the donut beam produced by the SPP through an optical system with ray transfer matrix $\mathbf{M} = \begin{pmatrix} A & B \\ C & D \end{pmatrix}$, we insert the initial field Eq. (2.11) into Eq. (2.16)

$$\begin{aligned} E(\rho,\phi,z) = &- i\frac{1}{\lambda_1 B} E_0 \frac{w_0}{w(z')} e^{ikz} e^{i\frac{kD\rho^2}{2B}} e^{-ikz'} e^{i\zeta(z')} \\ &\times \int_0^\infty \exp\left(-\frac{\rho'^2}{w^2(z')}\right) \exp\left(-i\frac{k\rho'^2}{2R(z')}\right) \exp\left(i\frac{kA\rho'^2}{2B}\right) \rho' d\rho' \\ &\times \int_0^{2\pi} \exp\left[\frac{-ik\rho\rho'\cos(\phi'-\phi)}{B}\right] \exp(i\phi') d\phi' \,. \end{aligned} \tag{2.17}$$

This integral can be solved analytically and the final analytical expression has the following form (for detail calculation for general topological charge l, see Appendix B)

$$\begin{aligned} E(\rho,\phi,z) =& \frac{1}{\lambda_1 B} E_0 \frac{w_0}{w(z')} (2\pi) \frac{\sqrt{\pi} b}{8a^{3/2}} e^{ikz} e^{i\frac{kD\rho^2}{2z}} e^{-ikz'} e^{i\zeta(z')} e^{i\phi} \\ & \times \exp\left(-\frac{b^2}{8a}\right) \left[I_0\left(\frac{b^2}{8a}\right) - I_1\left(\frac{b^2}{8a}\right) \right]. \end{aligned} \tag{2.18}$$

where I_m is a modified Bessel function of the first kind and m-th order and

$$\begin{aligned} a &= \left(\frac{1}{w^2(z')} + \frac{ik}{2R(z')} - \frac{iAk}{2B} \right), \\ b &= \frac{k\rho}{B}. \end{aligned} \tag{2.19}$$

The intensity distribution is then just given by

$$\mathcal{I}(\rho,\phi,z) = |E(\rho,\phi,z)|^2 . \tag{2.20}$$

In the following I investigate the propagation of the donut beam through free space and through a relevant lens system.

Free-space propagation

The ray transfer matrix for free space has the following form

$$M = \begin{pmatrix} 1 & z \\ 0 & 1 \end{pmatrix}. \tag{2.21}$$

For this case, Eq. (2.18) becomes

$$\begin{aligned} E(\rho,\phi,z) =& \frac{1}{\lambda_1 z} E_0 \frac{w_0}{w(z')} (2\pi) \frac{\sqrt{\pi} b}{8a^{3/2}} e^{ikz} e^{i\frac{k\rho^2}{2z}} e^{-ikz'} e^{i\zeta(z')} e^{i\phi} \\ & \times \exp\left(-\frac{b^2}{8a}\right) \left[I_0\left(\frac{b^2}{8a}\right) - I_1\left(\frac{b^2}{8a}\right) \right], \end{aligned} \tag{2.22}$$

with

$$\begin{aligned} a &= \left(\frac{1}{w^2(z')} + \frac{ik}{2R(z')} - \frac{ik}{2z} \right), \\ b &= \frac{k\rho}{z}. \end{aligned} \tag{2.23}$$

In Fig. 2.9, the experimental setup for measuring the beam profile of the donut beam after propagating through free space is shown. The laser source is an external cavity diode laser (ECDL). After passing through a Faraday isolator which avoids optical feedback, the output beam is split into two parts using a beam splitter. One is sent to a wavemeter for monitoring the wavelength of the laser and the other one is used for generating the donut beam. The latter is coupled into a single mode fiber in order to clean the mode, so that after

the fiber we have a clean Gaussian beam. Only a small percentage of the laser is needed to be coupled into the fiber, so that a telescope for mode matching is not necessary here. After the fiber the laser power is approximately 7.5 μW and the beam is linearly polarized. The beam is then passed through the SPP to generate the donut beam. The beam profile of the generated donut beam is measured using a beam profile camera and analysed using a computer software Spiricon. A typical image of the generated donut beam detected by the beam profile camera is shown in Fig. 2.6.

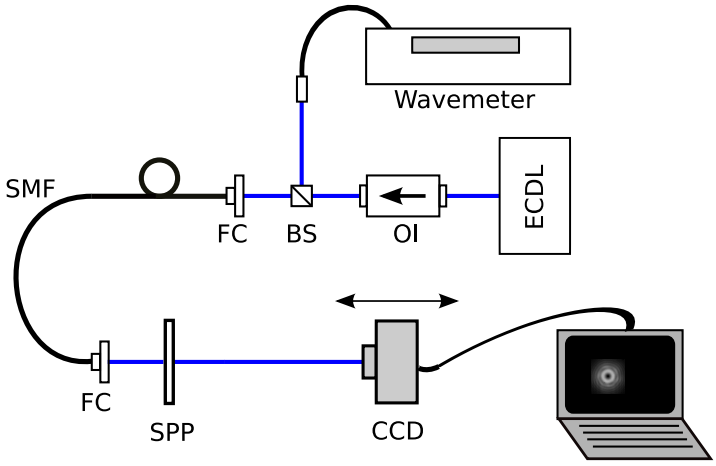

Figure 2.9: Experimental setup for measuring the beam profile of the generated donut beam after propagtion through free space. ECDL: external cavity diode laser; FI: Faraday isolator; BS: beam splitter; FC: fiber coupler; SMF: single-mode fiber; SPP: spiral phase plate; CCD: beam profile camera. After the fiber beam beam power $P = 7.5\,\mu$W. The postion of the CCD can be varied to measure the beam profile at different propagation distances.

In order to to determine the beam waist radius of the output Gaussian beam and its position, I measure the beam size size at two different positions, $w(z) \equiv w_1 = 1.198\,\text{mm}$ and $w(z + z_{\text{sep}}) \equiv w_2 = 1.275\,\text{mm}$, seperated at a distance $z_{\text{sep}} = 200\,\text{mm}$, using the beam profile camera. The beam waist radius can be then evaluated using the following formula

$$z_R = \frac{\lambda}{\pi} \frac{2 z z_{\text{sep}} + z_{\text{sep}}^2}{w_2^2 - w_1^2}\,, \tag{2.24}$$

$$w_0 = \sqrt{\frac{z_R \lambda}{\pi}}\,, \tag{2.25}$$

where the position z from the beam waist position is determined by solving the quadratic equation

$$\left(w_2^2 - w_1^2 + \frac{\lambda^2}{\pi^2} \frac{4 z_{\text{sep}}^2}{w_2^2 - w_1^2} \right) z^2 + \left(\frac{\lambda^2}{\pi^2} \frac{4 z_{\text{sep}}^3}{w_2^2 - w_1^2} - 2 w_1^2 z_{\text{sep}} \right) z + \left(\frac{\lambda^2}{\pi^2} \frac{z_{\text{sep}}^4}{w_2^2 - w_1^2} - w_1^2 z_{\text{sep}}^2 \right) = 0\,. \tag{2.26}$$

We finally obtain

$$\begin{aligned} z &= 2.138\,\text{m}\,, \\ z_R &= 1.366\,\text{m}\,, \\ w_0 &= 0.6\,\text{mm}\,. \end{aligned} \tag{2.27}$$

From the knowledge of the chosen position z relative to the beam waist position, the position where the SPP is located relative to the beam waist position, z' can also be determined. In this measurement the SPP is located at the position $z' = 1.4\,\mathrm{m}$ from the position of the beam waist.

In Fig. 2.10, the 1D radial intensity distributions of the donut beam behind the SPP at different propagation distances are shown, measured by varying the distance of the beam profile camera from the SPP. We observe that the beam profile changes dramatically upon propagation. At the beginning the beam has a high peak intensity and there are wiggles appearing in the intensity distribution. As the beam propagates the peak intensity decreases significantly and also the wiggles start to disappear.

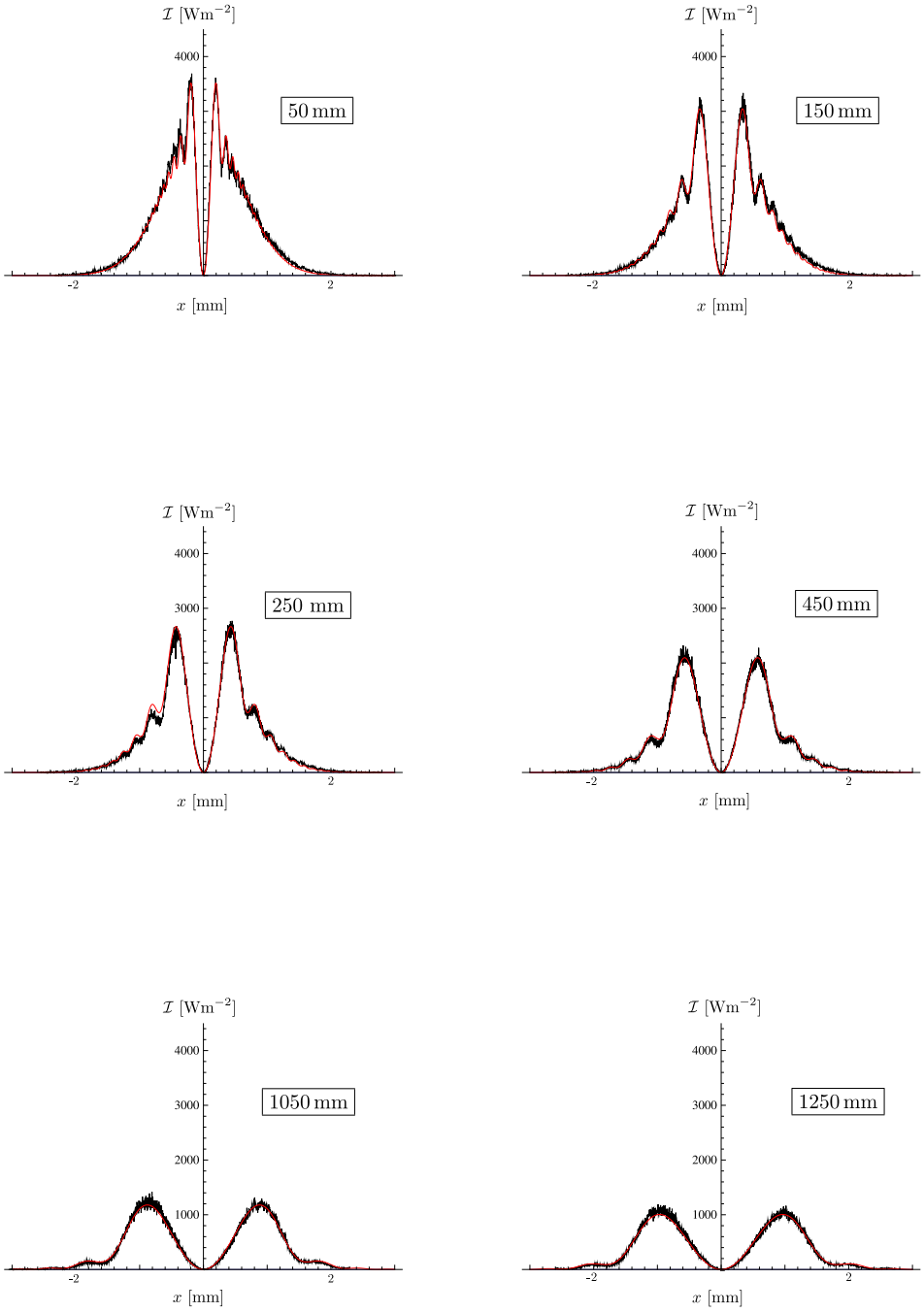

Figure 2.10: One-dimensional radial intensity distributions of donut beams generated by the SPP after propagating through free space at different propagation distances. The red and black curves represent calculated and measured intensity distributions, respectively. The parameters of the incident Gaussian beam are: $w_0 = 0.6\,\text{mm}$, $\lambda = 849.9\,\text{mm}$, $P = 7.5\,\mu\text{W}$. The SPP is illuminated at the distance $z' = 1.4\,\text{m}$ from the position of the beam waist.

Propagation through a lens system

We are particularly interested in the lens system sketched in Fig. 2.11. This is the lens system the beam has to pass through when integrated in the main experiment [33]. The total

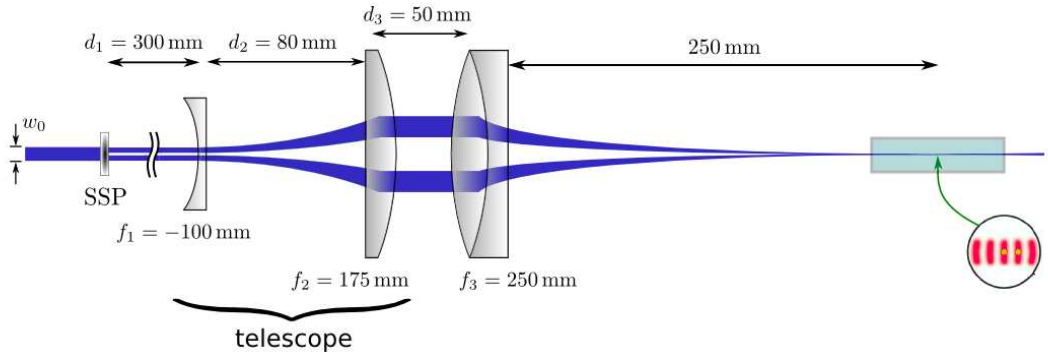

Figure 2.11: Schematic representation of the lens system used in the main experiment to focus down the lattice and the donut beams. Lens 1 and lens 2 form a Galilean telescope.

ray transfer matrix of the lens system can be obtained by taking the matrix multiplication of the individual relevant ray transfer matrices

$$\begin{aligned}\mathbf{M}_{\mathrm{tot}} &= \mathbf{M}_{\mathrm{free}_1} \cdot \mathbf{M}_{\mathrm{tel}} \cdot \mathbf{M}_{\mathrm{free}_3} \cdot \mathbf{M}_{\mathrm{lens}_3} \cdot \mathbf{M}_{\mathrm{free}} \\ &= \begin{pmatrix} 1 & d_1 \\ 0 & 1 \end{pmatrix} \cdot \begin{pmatrix} -\frac{f_2}{f_1} & f_1 + f_2 \\ 0 & -\frac{f_1}{f_2} \end{pmatrix} \cdot \begin{pmatrix} 1 & d_3 \\ 0 & 1 \end{pmatrix} \cdot \begin{pmatrix} 1 & 0 \\ -\frac{1}{f_3} & 1 \end{pmatrix} \cdot \begin{pmatrix} 1 & z \\ 0 & 1 \end{pmatrix} \\ &= \begin{pmatrix} -\frac{f_2\left(1-\frac{z}{f_3}\right)}{f_1} & -\frac{d_1 f_2\left(1-\frac{z}{f_3}\right)}{f_1} + (f_1+f_2)\left(1-\frac{z}{f_3}\right) - \frac{f_1\left(z+d_2\left(1-\frac{z}{f_3}\right)\right)}{f_2} \\ \frac{f_2}{f_1 f_3} & -\frac{f_1\left(1-\frac{d_2}{f_3}\right)}{f_2} + \frac{d_1 f_2}{f_1 f_3} - \frac{f_1+f_2}{f_3} \end{pmatrix}. \end{aligned} \tag{2.28}$$

The experimental setup for measuring the beam profile of the donut beam after propagating through the lens system is illustrated in Fig. 2.12. It is the same to that for free space propagation with the additional lens system in between the SPP and the beam profile camera.

The beam profile at different propagation distances behind the last focusing lens is shown in Fig. 2.14. In order to get a good fitting between the calculated and measured intensity distributions, the theoretical distances have been commonly shifted within 15 mm. This adjustment is justified since we do not know the exact position of the chip of the CCD camera neither the real focal length of each lens. The beam profile at the focal plane of the last lens cannot be measured since the beam diameter at this position is too small to be resolved by the CCD camera. The calculated one 1D radial intensity distribution at this position is illustrated in Fig. 2.13.

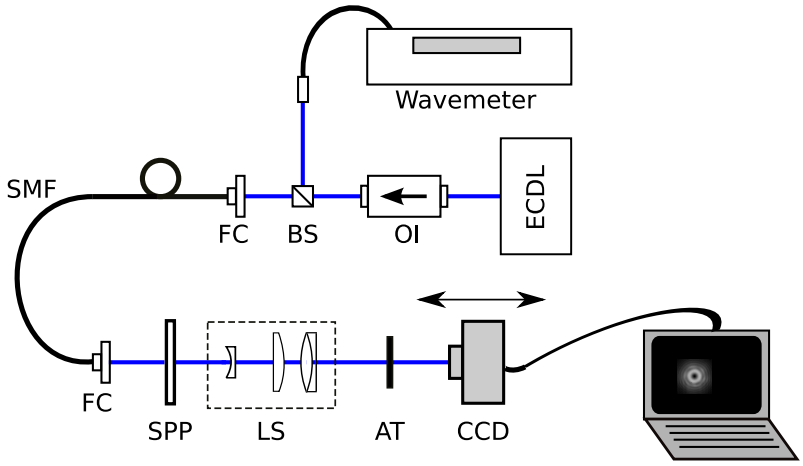

Figure 2.12: Experimental setup for measuring the beam profile of the generated donut beam after propagtion through the lens system. ECDL: external cavity diode laser; OI: optical isolator; BS: beam splitter; FC: fiber coupler; SMF: single-mode fiber; SPP: spiral phase plate; CCD: beam profile camera. The position of the CCD can be varied to measure the beam profile at different propagation distances.

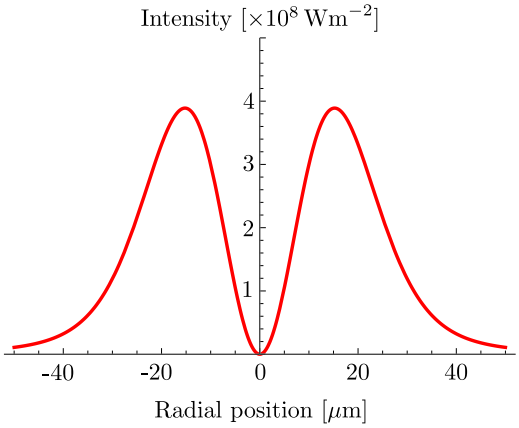

Figure 2.13: Calculated 1D radial intensity distribution at the focal plane of the last lens.

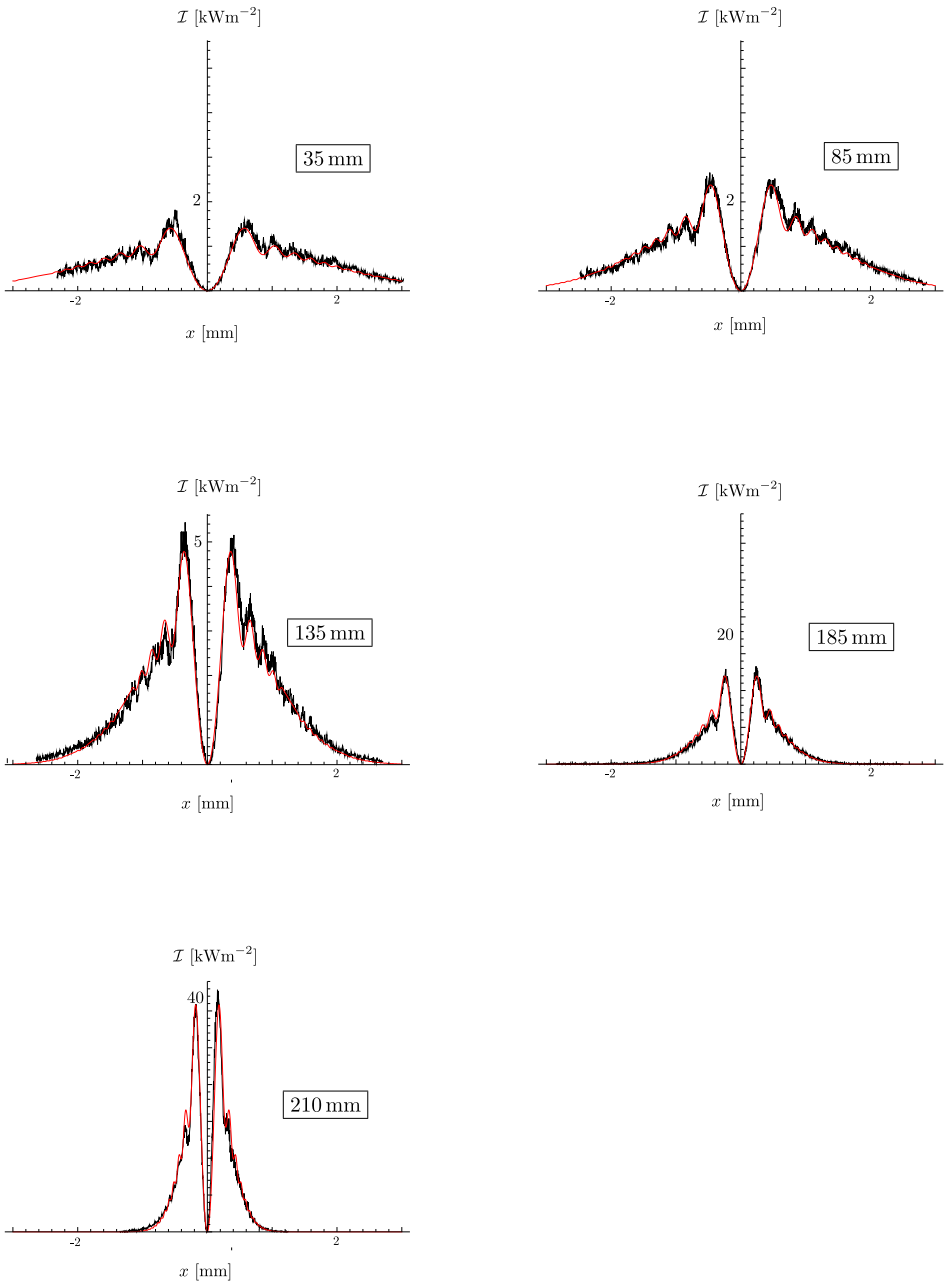

Figure 2.14: One dimensional radial intensity distributions of donut beams generated by the SPP after propagating through the lens system at different propagation distances. The red and black curves represent calculated and measured intensity distributions, respectively. The parameters of the incident Gaussian beam are: $w_0 = 0.6\,\text{mm}$, $\lambda = 850\,\text{mm}$, $P = 7.5\,\mu\text{W}$. The SPP is illuminated at the distance $z' = 1.4\,\text{m}$ from the position of the beam waist. Due to the limitation of the camera resolution the beam profile at the focal plane of the focusing lens ($z = 250\,\text{mm}$) cannot be measured.

2.2.3 Wavelength dependence

So far we have only consider illumination of the SPP with wavelength $\lambda_1 = 849.9\,\text{nm}$ which causes the SPP to introduce the topological charge $l = 1$ to the incident beam. We have calculated the intensity distribution behind the SPP which has a perfect donut shape. It is also instructive to see what happens if the SPP is illuminated with a Gaussian beam with a wavelength $\lambda_\alpha \neq \lambda_1$.

When illuminated with a Gaussian beam with the wavelength $\lambda_\alpha \neq \lambda_1$, the SPP introduces a topological charge α to the beam which is not equal to 1 but fractional. This topological charge can be calculated from Eq. (2.8). The topological charges introduced to incident beams with several different wavelengths are listed in Table 2.2.

Wavelength, λ_α [nm]	Topological charge, α
848	1.0022
849	1.0011
851	0.9987
852	0.9975
858.48	0.9900
867.24	0.9800

Table 2.2: Topological charge α introduced by the SPP when illuminated with a beam of wavelength $\lambda_\alpha \neq \lambda_1 = 849.9\,\text{nm}$.

Since α is fractional, the integration over the azimuthal angle in Eq. (B.4) does not take a closed form. We can however express the phase factor $\exp(i\alpha\phi)$ as a Fourier series [36]

$$\exp(i\alpha\phi) = (-1)^\alpha \frac{\sin(\pi\alpha)}{\pi} \sum_{m=-\infty}^{m-\infty} \frac{\exp(im\phi)}{\alpha - m}. \tag{2.29}$$

This enables us to analytically carry out the integration over the azimuthal angles in Eq. (B.4), which gives us the following analytical expression for the field amplitude for a beam with wavelength $\lambda_\alpha \neq \lambda_1$

$$\begin{aligned} E_\alpha(\rho,\phi,z) = \sum_{m=-\infty}^{m-\infty} (-i)^{|m|+1} \frac{1}{\lambda_\alpha B} E_0 \frac{w_0}{w(z')} (2\pi) \frac{\sqrt{\pi} b}{8a^{3/2}} e^{ikz} e^{i\frac{kD\rho^2}{2z}} e^{-ikz'} e^{-i\zeta(z')} \\ \times (-1)^\alpha \frac{\sin(\pi\alpha)}{\pi} \frac{e^{im\phi}}{\alpha - m} e^{-\frac{b^2}{8a}} \left[I_{\frac{1}{2}|m|-\frac{1}{2}}\left(\frac{b^2}{8a}\right) - I_{\frac{1}{2}|m|+\frac{1}{2}}\left(\frac{b^2}{8a}\right) \right]. \end{aligned} \tag{2.30}$$

The calculated and measured intensity distributions for generated beams with different fractional topological charges are shown in Fig. 2.15. The appearence of discontinuities in the intensity distributions implies that the beams are no longer suitable to be used to trap atoms.

Nevertheless, in the wavelength of our interest, which is in between 840 nm to 852 nm, a sufficiently good donut beam can still be obtained, as shown in Fig. 2.16. This is due to the fact that in this range, the topological charge $\alpha \approx 1$. If we use the following limiting

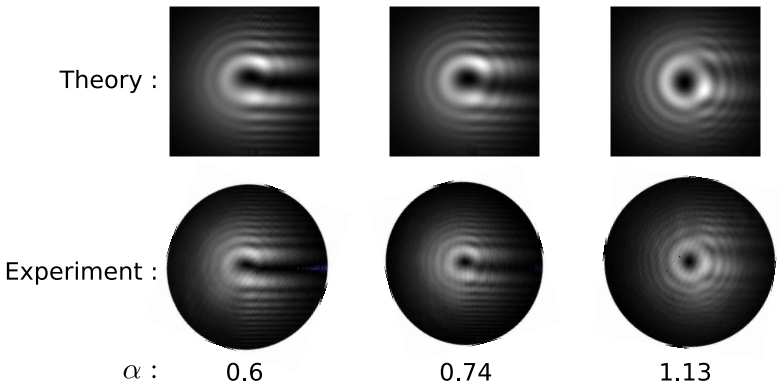

Figure 2.15: Theoretical and experimental intensity distributions of donut beams with fractional topological charges α.

form

$$\lim_{\alpha\to 1}\left[\frac{(-1)^{\alpha}\sin(\alpha\pi)}{\pi(\alpha-1)}\right]=\delta_{\alpha 1}\,, \tag{2.31}$$

Eq. (2.30) becomes

$$\begin{aligned}E_{\alpha}(\rho,\phi,z)\overset{\alpha\to 1}{\approx}&\frac{1}{\lambda_{\alpha}B}E_0\frac{w_0}{w(z')}(2\pi)\frac{\sqrt{\pi}b}{8a^{3/2}}e^{ikz}e^{i\frac{kD\rho^2}{2z}}e^{-ikz'}e^{i\zeta(z')}e^{il\phi}\\&\times\exp\left(-\frac{b^2}{8a}\right)\left[I_0\left(\frac{b^2}{8a}\right)-I_1\left(\frac{b^2}{8a}\right)\right],\end{aligned} \tag{2.32}$$

which is just the same as the field amplitude of a perfect donut beam with topological charge $l=1$ (see Eq. (2.18))

However, for a donut beam with the wavelength $\lambda_{\alpha}\neq\lambda_1$, the light intensity on the beam axis is not equal to zero. On the beam axis ($\rho=0$), the only non-zero contribution to the sum of Eq. (2.30) comes from $m=0$, so that the field amplitude at the center reads

$$E_{\alpha}(0,\phi,z)=\frac{-i}{2a}\frac{2\pi}{\lambda_{\alpha}B}E_0\frac{w_0}{w(z')}e^{ikz}e^{-ikz'}e^{-i\zeta(z')}(-1)^{\alpha}\frac{\sin(\pi\alpha)}{\pi\alpha}. \tag{2.33}$$

Thus,

$$\mathcal{I}_{\alpha}(0,\phi,z)=\frac{1}{4|a|^2}\left(\frac{2\pi}{\lambda_{\alpha}B}\right)^2E_0^2\left(\frac{w_0}{w(z')}\right)^2|(-1)^{\alpha}|^2\,\frac{\sin^2(\pi\alpha)}{(\pi\alpha)^2} \tag{2.34}$$

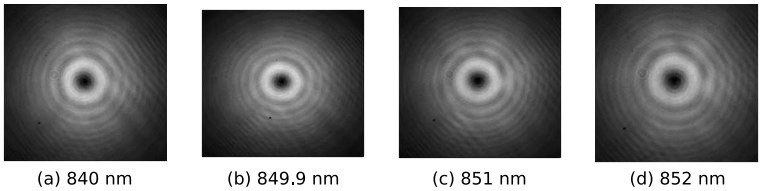

Figure 2.16: Intensity distributions of donut beams generated by illuminating the SPP with incident beams of different wavelengths in the range between 840 nm to 852 nm. A sufficiently good donut beam can be obtained in this wavelength range.

2.2.4 Misalignment of the SPP

In practice the configuration of the SPP and the incident Gaussian beam is inevitably imperfect, i.e. the optical axis of the beam is not perfectly at the center of the SPP and also there should be a small incident angle. This effects have been extensively studied in [37]. It was shown that for small incident angles the modification caused to the intensity pattern of the diffracted beam is negligeble.

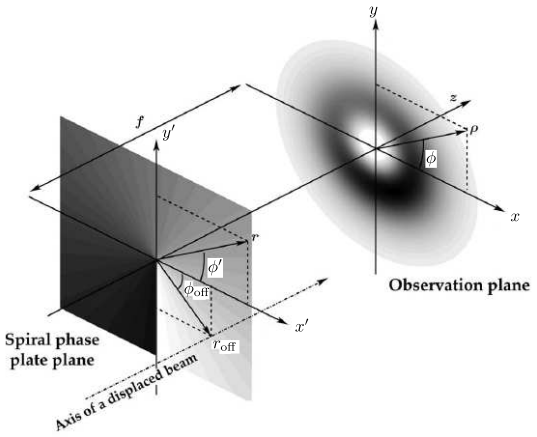

Figure 2.17: Lateral misaligment of the SPP.

For off-axis lateral displacements where the SPP is displaced at the position $(r_{\text{off}}, \theta_{\text{off}})$ from the center of the incident Gaussian beam, the intensity of the diffracted beam is given by

$$\begin{aligned} E(\rho,\phi,z) =& \frac{1}{\lambda_1 B} E_0(2\pi) \frac{\sqrt{\pi} b}{8a^{3/2}} e^{ikz} e^{i\frac{kD\rho^2}{2z}} e^{-\frac{r_{\text{off}}^2}{w_0^2}} e^{il\gamma} \\ & \times \exp\left(-\frac{b^2}{8a}\right)\left[I_0\left(\frac{b^2}{8a}\right) - I_1\left(\frac{b^2}{8a}\right)\right]. \end{aligned} \tag{2.35}$$

with

$$\begin{aligned} a &= \left(\frac{1}{w_0^2} - \frac{iAk}{2B}\right) \\ b &= \frac{k}{B}\frac{w_0 Q}{\sqrt{2}} \\ w_0^2 Q^2 &= 2\rho^2 - 4\left(\frac{B}{z_R} r_{\text{off}}\right)^2 + 4i\frac{B}{z_R} r_{\text{off}} \cos(\phi - \phi_{\text{off}}) \\ \tan\gamma &= \frac{\rho\sin\phi + i\frac{B}{z_R} r_{\text{off}} \sin\phi_{\text{off}}}{\rho\cos\phi + i\frac{B}{z_R} r_{\text{off}} \cos\phi_{\text{off}}} \end{aligned} \tag{2.36}$$

In [37] it was shown that in the observation plane (x, y), the dark region of the beam is located neither on the beam axis nor in the origin of the (x', y') plane, but shifted to a position

$$\rho = r_{\text{off}} \frac{B}{z_R}, \qquad \phi = \phi_{\text{off}} - \text{sgn}(l)\frac{\pi}{2}. \tag{2.37}$$

Consequently, the dark region is not fixed at the z axis but moves away from it along the straight line orthogonal to the incident beam displacement, as the beam propagates. This effect is illustrated in Fig. 2.18 for an extreme beam displacement.

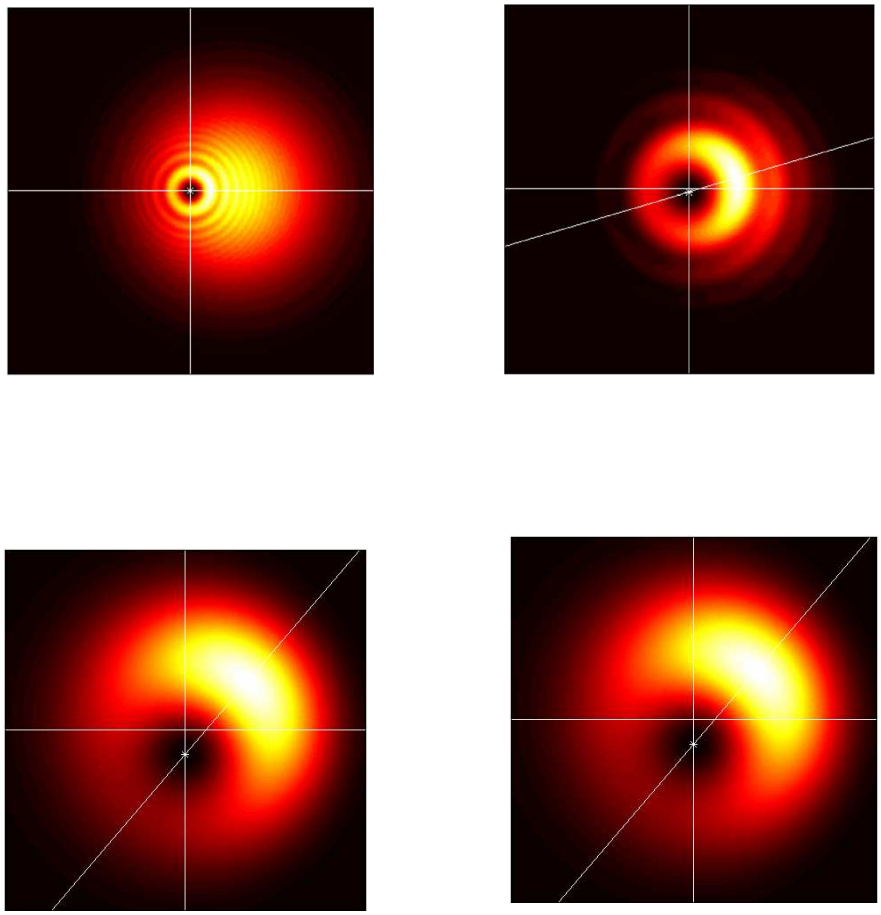

Figure 2.18: Calculated intensity distributions of off-axial donut beams at different propagation distances [37]. The dark region is not fixed at the z axis but moves away from it along the straight line orthogonal to the incident beam displacement, as the beam propagates.

A part from the modification of the position of the dark region which is embedded in the modification of the parameter b, the expression of Eq. (2.35) has a similar form as Eq. (2.18). This implies that in the vicinity of the dark region the beam preserves its circular symmetry and remains locally isotropic, just like in the case of a non-shifted incident beam.

Chapter 3

Neutral atoms in a donut beam

3.1 Forces on atoms in the donut beam

3.1.1 Dipole potential

Consider an atom placed in a light field $\boldsymbol{E}$. This light field induces an atomic dipole moment $\hat{\boldsymbol{d}}$ which then interacts with the light field. The corresponding interaction Hamiltonian reads $\hat{H}' = -\hat{\boldsymbol{d}} \cdot \boldsymbol{E}$. It yields a shift in the energy levels of the atom, the so-called AC-Stark shift. In the rotating wave approximation, from second-order perturbation theory the energy shift of a state $|i\rangle$ can be calcualted by

$$\Delta E_i = \frac{1}{4} \sum_{j \neq i} \frac{|\langle j|\hat{\boldsymbol{d}} \cdot \boldsymbol{E}_0|i\rangle|^2}{\hbar\,(\omega_L - \omega_{ij})}\,. \tag{3.1}$$

From this relation, a general expression for the light shift of a ground state with total angular momentum F and magnetic quantum number m_F can be derived. For an alkali atom with ground state $J = 1/2$ and excited states $J' = 1/2$ and $J' = 3/2$, the energy shift reads [38]

$$\Delta E_g = \frac{\pi c^2}{2} \left(\frac{\Gamma_{3/2}}{\omega_{3/2}^3 \Delta_{3/2}} (2 + \mathcal{P} g_F m_F) + \frac{\Gamma_{1/2}}{\omega_{1/2}^3 \Delta_{1/2}} (1 - \mathcal{P} g_F m_F) \right) \mathcal{I}\,. \tag{3.2}$$

Here $\Delta_{J'} = \omega_L - \omega_{J'}$ is the detuning of the laser frequency ω_L from the $6^2P_{J'}$ excited states, the transition frequencies and spontaneous decay rates of which are denoted by $\omega_{J'}$ and $\Gamma_{J'}$, respectively. g_F denotes the Lande factor, $\mathcal{I} = |\boldsymbol{E}|^2$ the intensity of the light field. $\mathcal{P}$ characterizes the polarization state of the beam and is defined as

$$\mathcal{P} = \begin{cases} 0 & \text{for } \pi\text{-polarized light} \\ \pm 1 & \text{for } (\sigma_\pm)\text{- polarized light.} \end{cases} \tag{3.3}$$

According to Eq. (3.2), the light shift is directly proportionally to the light intensity. Thus, in a light field with an inhomogeneous intensity distribution the atom feels a position-dependant light shift, resulting in a potential for the atom which also refer to as dipole potential (Fig. 3.1). Depending on whether the light frequency is detuned below (red-detuned) or above (blue-detuned) the atomic transitions, the atom can be attracted towards the intensity maxima or minima.

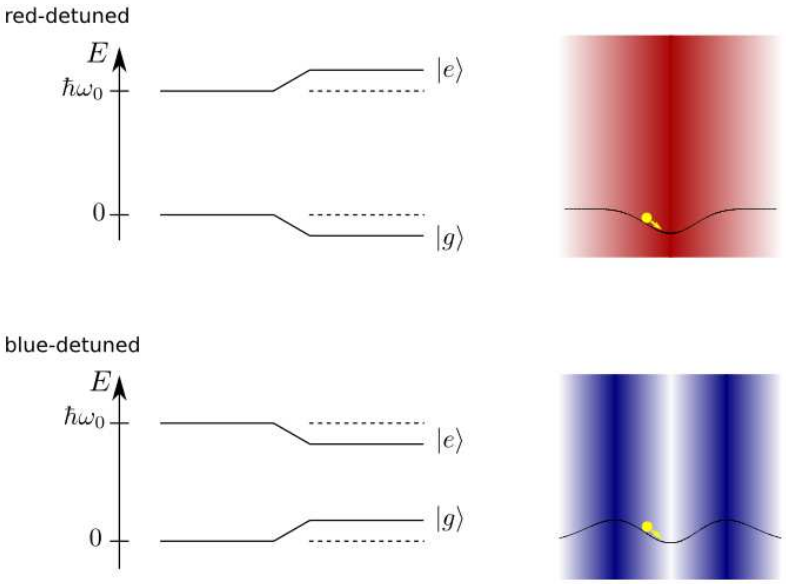

Figure 3.1: Illustration of the light shift of the energy levels of a two-level atom. The light shift is proportional to the laser intensity whereas its sign depends on the detuning Δ. In red-detuned case the atom is attracted to the high intensity region. In blue-detuned case the atom is repelled from the intensity maximum.

3.2 Blue-detuned donut beam for Cs

Having briefly discussed the basic mechanism which allows neutral atoms to be trapped in a gradient light field, we now focus on trapping of Cs atoms in the donut beam discussed in the previous chapter. The donut beam is blue-detuned with respect to the D_1 and D_2 line, so that atoms are trapped in the intensity minimum in its center. After being generated by the SPP, the donut beam passes through a lens system, as illustrated in Fig. 2.11. The Cs atoms are trapped at the focal plane of the last lens. Thus, the intensity distribution and the dipole potential at this position will be our main concern. The corresponding total ray transfer matrix of our problem is given by

$$\mathbf{M}_{\text{tot}} = \begin{pmatrix} 0 & \frac{f_3}{\mathcal{M}} \\ -\frac{\mathcal{M}}{f_3} & -\frac{f_1\left(1-\frac{d_2}{f_3}\right)}{f_2} + \frac{d_1 f_2}{f_1 f_3} - \frac{f_1+f_2}{f_3} \end{pmatrix} . \tag{3.4}$$

Assuming the SPP is located at the position of the waist of the incident Gaussian beam, the intensity distribution of the donut beam at the position of the atoms can be then written as (cf. Eq. (2.18)-Eq. (2.20))

$$\mathcal{I}_{\text{blue}}(\rho) = E_0^2 \frac{\pi k^4 w_0^6}{64 B^4} \rho^2 \exp\left(-2\xi\rho^2\right) \left[I_0\left(\xi\rho^2\right) - I_1\left(\xi\rho^2\right)\right]^2 , \tag{3.5}$$

with

$$\xi = \frac{k^2 w_0^2}{8B^2} , \tag{3.6}$$

$$B = \frac{f_3}{\mathcal{M}} . \tag{3.7}$$

When placed in the blue detuned donut beam, a Cs atom sees a dipole potential of the form

$$\begin{aligned} U_{\text{blue}}(\rho) &= \frac{\pi c^2}{2}\left(\frac{\Gamma_{\text{D2}}}{\omega_{\text{D2}}^3\Delta_{\text{D2}}}(2+\mathcal{P}g_F m_F)+\frac{\Gamma_{\text{D1}}}{\omega_{\text{D1}}^3\Delta_{\text{D1}}}(1-\mathcal{P}g_F m_F)\right)\mathcal{I}_{\text{blue}}(\rho) \\ &= \mathcal{C}E_0^2\frac{\pi k^4 w_0^6}{64B^4}\rho^2\exp\left(-\xi\rho^2\right)\left[I_0\left(\xi\rho^2\right)-I_1\left(\xi\rho^2\right)\right]^2 . \end{aligned} \tag{3.8}$$

Here we define

$$\mathcal{C} \equiv \frac{\pi c^2}{2}\left(\frac{\Gamma_{\text{D2}}}{\omega_{\text{D2}}^3\Delta_{\text{D2}}}(2+\mathcal{P}g_F m_F)+\frac{\Gamma_{\text{D1}}}{\omega_{\text{D1}}^3\Delta_{\text{D1}}}(1-\mathcal{P}g_F m_F)\right) , \tag{3.9}$$

which acts as a scaling factor between the light intensity and the dipole potential. The resulting potential in the (x, y)-plane is plotted in Fig. 3.2.

For nonlinearly polarized beams, the terms contaning the Lande factor g_F and the magnetic quantum number m_F in Eq. (3.9) are non-zero. Consequently, the potential is dependent on the state of the atom. The situation is illustrated in Fig. 3.3. For the analysis that follows, the beam size radius of the Gaussian beam before the SPP is assumed to be $w_0 = 3\,\text{mm}$, while the beam is linearly polarized unless otherwise noted.

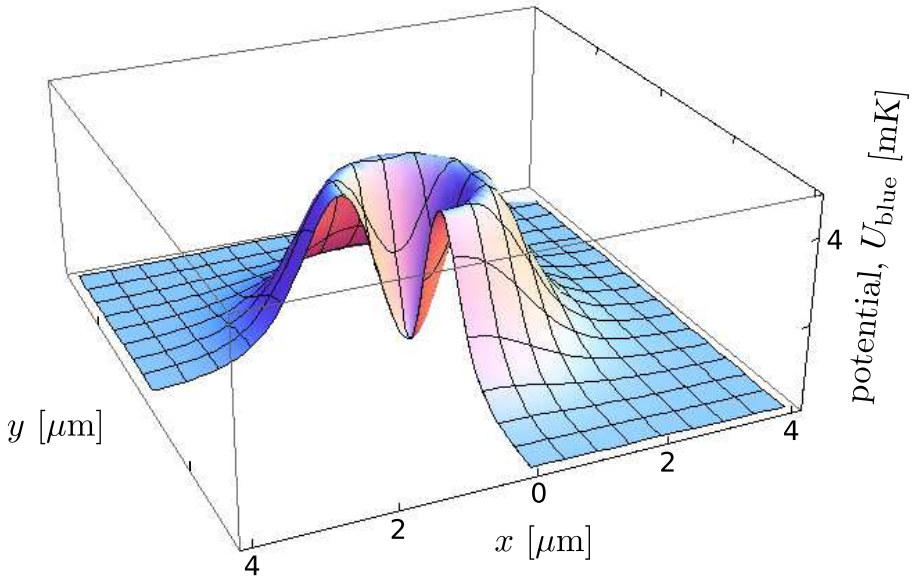

Figure 3.2: Calculated dipole potential formed by the donut beam in the plane perpendicular to the optical axis. The potential depth is about 4 mK which is sufficiently deep to trap Cs atoms cooled to approximately 10 μK by optical molasses.

3.2.1 Harmonic approximation of the donut dipole potential

The dynamics of an atom trapped in the conservative dipole potential is conveniently described in terms of the formalism of a harmonic oscillator which has been well studied in

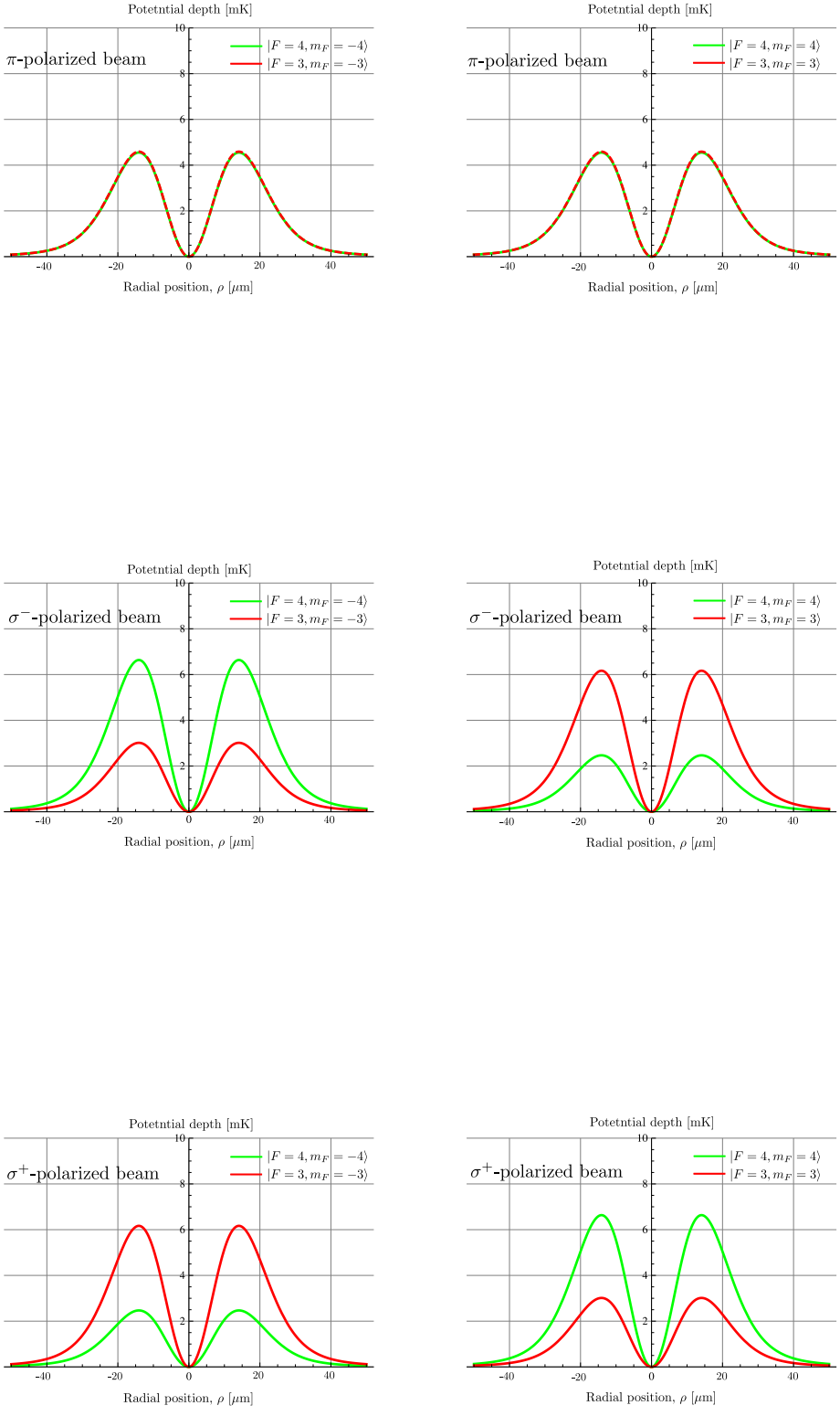

Figure 3.3: Polarization dependence of the dipole potential for different atomic states.

many standard quantum mechanics textbooks (see e. g. Ref. [39]). In the following, we apply the harmonic approximation to the donut dipole potential. For this, we first investigate the dipole potential near the beam axis. By making use of the following limiting forms [43]

$$I_\nu(\gamma) \approx \frac{(\gamma/2)^\nu}{\Gamma(\nu+1)} \quad \text{as } \gamma \to 0, \tag{3.10}$$

and

$$\exp(\kappa) \approx 1 + \kappa \quad \text{as } \kappa \to 0, \tag{3.11}$$

Eq. (3.8) becomes

$$\begin{aligned} U_{\text{blue}}(\rho) &\approx \mathcal{C}E_0^2 \frac{\pi k^4 w_0^6}{64B^4} \rho^2 \left(1 - 2\xi\rho^2\right) \left[\left(\frac{\left(\frac{\xi}{2}\rho^2\right)^0}{\Gamma(1)} \right) - \left(\frac{\left(\frac{\xi}{2}\rho^2\right)^1}{\Gamma(2)} \right) \right] \\ &\approx \mathcal{C}E_0^2 \frac{\pi k^4 w_0^6}{64B^4} \rho^2 \left(1 - 2\xi\rho^2\right) \left(1 - \frac{\xi}{2}\rho^2\right)^2 \\ &\approx \mathcal{C}E_0^2 \frac{\pi k^4 w_0^6}{64B^4} \left[\rho^2 + \mathcal{O}(\rho^4)\right] \end{aligned} \tag{3.12}$$

as $\rho \to 0$. Here $\Gamma(\nu)$ is the Gamma function. Keeping only the leading term in this expansion, we obtain the harmonic approximation to the dipole potential. The approximation holds for an atom whose energy is much smaller than the potential depth. This is exactly true in our case (see Fig. 3.2).

By comparing Eq. (3.12) with the potential of a harmonic oscillator

$$V_{\text{harm}}(\rho) = \frac{1}{2} m \omega_{\text{harm}}^2 \rho^2 \tag{3.13}$$

we infer for the radial oscillation frequency

$$\Omega_{\text{rad}} = \sqrt{\frac{\mathcal{C}P}{16m}} \frac{\mathcal{M}^2}{f_3^2} k^2 w_0^2 \,. \tag{3.14}$$

From this expression, we deduce that the oscillation frequency scales with the power as $\Omega_{\text{rad}} \propto \sqrt{P}$, whereas with the beam waist radius of the incident Gaussian beam as

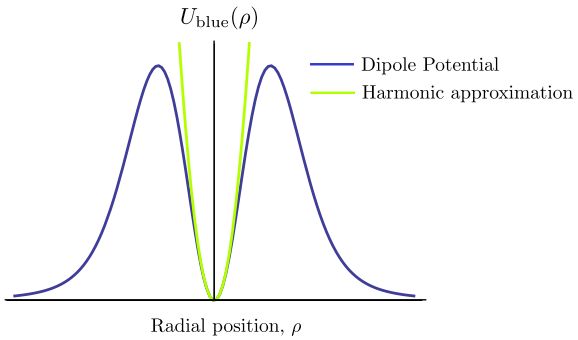

Figure 3.4: Harmonic approximation to the donut dipole potential.

$\Omega_{\mathrm{rad}} \propto w_0^2$, as illustrated in Fig. 3.5 and Fig. 3.6. For this reason, the more effective way to increase the oscillation frequency is through increasing the beam waist radius of the incident Gaussian beam w_0.

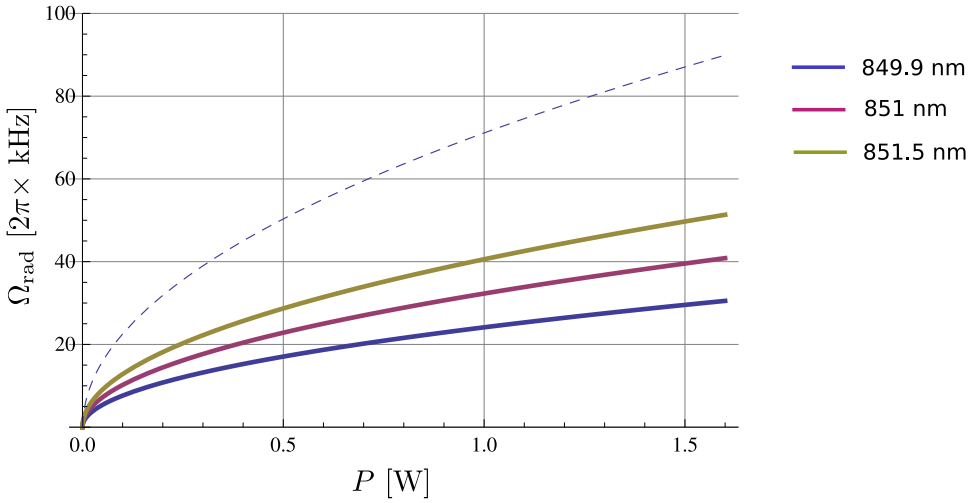

Figure 3.5: Power dependence of the oscillation frequency for different wavelengths. The beam waist radius of the Gaussian beam is fixed ($w_0 = 3\,\mathrm{mm}$). The dash line illustrates the calculated oscillation frequency for a telescope with magnification $\mathcal{M} = 3$ ($\lambda = 849.9\,\mathrm{nm}$).

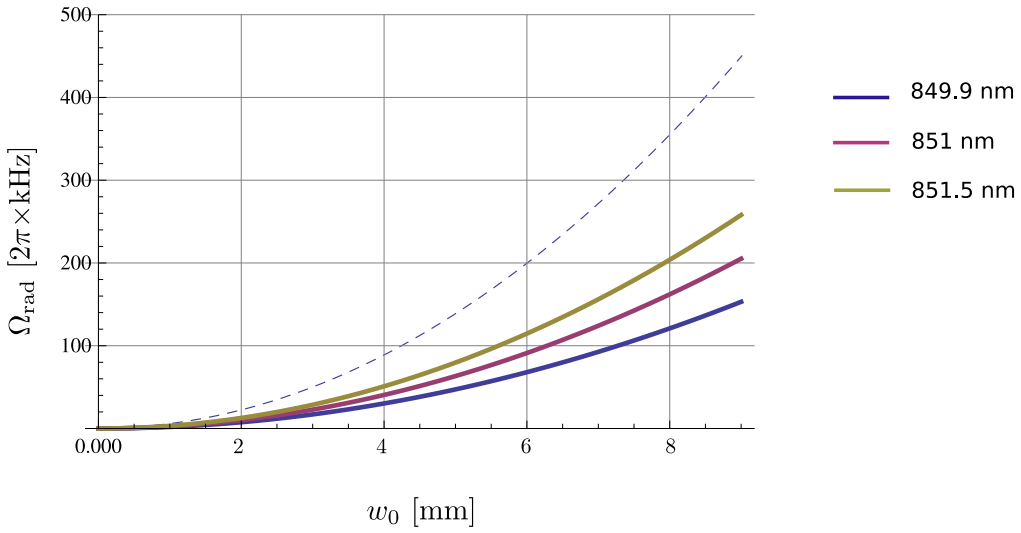

Figure 3.6: Dependence of the oscillation frequency on the beam waist radius of the incident Gaussian beam. The power is assumed to be $P = 0.5\,\mathrm{W}$. The dash line illustrates the calculated oscillation frequency for a telescope with magnification $\mathcal{M} = 3$ ($\lambda = 849.9\,\mathrm{nm}$).

In principle the size of the incident Gaussian beam can be increased arbitrarily. However, due to the limited diameter of the optical elements in the potential beam path, the beam size is limited to the size of this elements. Replacing this elements, for example a high extinction-ratio polarizer, with new ones with larger size might be very costly. A less

expensive alternative to increase the oscillation frequency is by replacing the lens system itself. This effect can directly be seen form Eq. (3.14) where the magnification of the telescope appears as $\Omega_{\text{rad}} \propto \mathcal{M}^2$ and the focal length of the last lens as $\Omega_{\text{rad}} \propto 1/f_3^2$. The effect of replacing the existing telescope with a one with magnification $\mathcal{M} = 3$, is exemplarily illustrated by the dash lines in Fig. 3.5 and Fig. 3.6.

3.2.2 Two-dimensional harmonic potential

From the preceding section we deduce that for low temperatures, the resulting dipole potential for an atom in the blue-detuned donut beam can be approximated to a two dimensional harmonic potential. In this section, I investigate some quantum mechanical properties of a two dimensional harmonic oscillator, showing that the energy eigenvalues are degenerate and also the oscillator posseses well-defined quantized orbital angular momentum.

Energy levels and stationary states

A particle in a two dimensional harmonic potential is described by the Schrödinger equation

$$\hat{\mathcal{H}}|\psi_{N_X,N_Y}\rangle = E_{N_X,N_Y}|\psi_{N_X,N_Y}\rangle \tag{3.15}$$

with

$$\hat{\mathcal{H}} = \frac{1}{2m}(\hat{P}_X^2 + \hat{P}_Y^2) + \frac{1}{2}m\Omega_{\text{rad}}^2(\hat{X}^2 + \hat{Y}^2)\,. \tag{3.16}$$

Here $\hat{P}$ and $\hat{X}$ denote the momentum and position operators of the center of mass motion of the particle, respectively.

The eigenstates of the Hamiltonian have the following form [39]

$$\psi_{N_X,N_Y}(X,Y) = \frac{\beta}{\sqrt{\pi(2)^{N_X+N_Y}(N_X)!(N_Y)!}}\exp\left[-\beta^2(X^2+Y^2)\right]H_{N_X}(\beta X)H_{N_Y}(\beta Y) \tag{3.17}$$

with the corresponding eigenvalues

$$\begin{aligned} E_{N_X,N_Y} &= \left(N_X + \frac{1}{2}\right)\hbar\Omega_{\text{rad}} + \left(N_Y + \frac{1}{2}\right)\hbar\Omega_{\text{rad}} \\ &= (N_X + N_Y + 1)\,\hbar\Omega_{\text{rad}} \\ &= (N+1)\,\hbar\Omega_{\text{rad}}\,, \qquad N = 0,1,2,\ldots \end{aligned} \tag{3.18}$$

Here H_{N_i} denote the Hermite polynomials (not to be confused with the Hamiltonian) and $\beta = \sqrt{\frac{m\Omega_{\text{rad}}}{\hbar}}$. In contrast to the one-dimensional case, the energy of the ground state is equal to $\hbar\Omega_{\text{rad}}$ rather than $\frac{1}{2}\hbar\Omega_{\text{rad}}$. The energy levels are degenerate since several stationary states can have the same value of energy. For example, the stationary states

$$|\psi_{N_x=3,N_y=0}\rangle, |\psi_{N_x=2,N_y=1}\rangle, |\psi_{N_x=1,N_y=2}\rangle, |\psi_{N_x=0,N_y=3}\rangle \tag{3.19}$$

have the same value of energy which is equal to $4\hbar\omega$. In general, the degree of degeneracy of the level E_N is equal to:

$$g_N = N + 1\,. \tag{3.20}$$

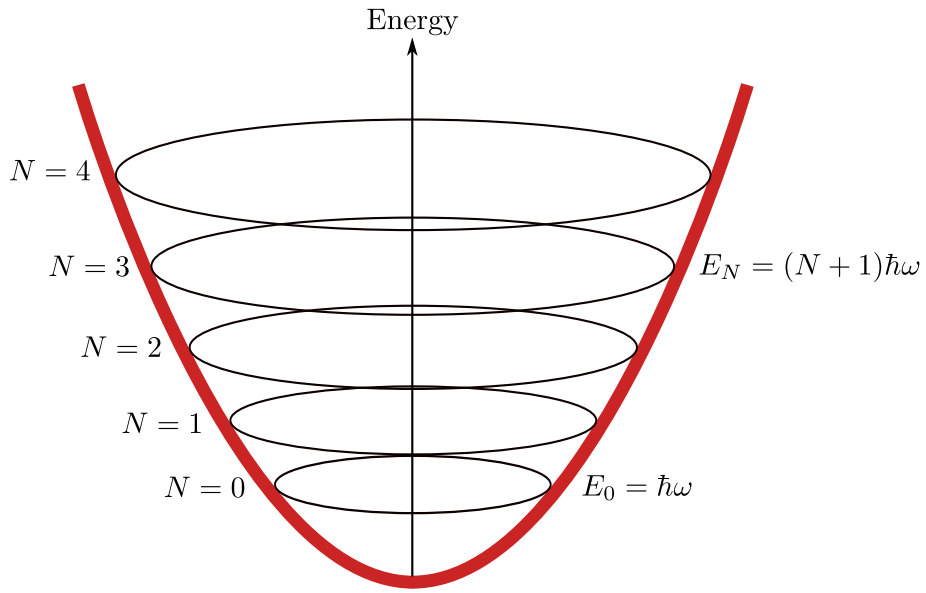

Figure 3.7: Illustration of the two-dimensional quantum mechanical harmonic potential, showing the quantization of energy.

Orbital angular momentum

In the two dimensional harmonic oscillator, the potential energy is invariant under rotation about the z-axis (the beam axis), so is the Hamiltonian. According to Noether's theorem, this symmetry implies the existence of a conserved quantity which turns out to be the component L_z of the angular momentum. Consequently, the Hamiltonian of the system commutes with L_z

$$[\mathcal{H}, L_z] = 0. \tag{3.21}$$

It is therefore possible to find eigenstates which are common to $\mathcal{H}$ and L_z. Such eigenstates have the following form [39]

$$\psi_{N,M}(R,\Phi) = \frac{\beta}{\sqrt{\pi}} \sqrt{\frac{\left(\frac{N-|M|}{2}\right)!}{\left(\frac{N+|M|}{2}\right)!}} (\beta R)^{|M|} L^{|M|}_{(N-|M|)/2}[(\beta R)^2] \exp\left(-\frac{(\beta R)^2}{2}\right) \exp\left(iM\Phi\right). \tag{3.22}$$

In this alternative representation, the quantum state of the oscillator is labelled by two quantum numbers N and M. Here, N represents the energy of the atom whose values are $(N+1)\hbar\Omega_{\text{rad}}$, whereas M determines the angular momentum of the oscillator, the eigenvalues of which are $M\hbar$. For a given N, there are $(N+1)$-degenerate angular momentum states with quantum number

$$M = N, N-2, N-4, \cdots, -N+4, -N+2, -N\,. \tag{3.23}$$

By employing an auxiliary donut beam carrying a well-defined orbital angular momentum [24], it would be possible to manipulate the angular momentum of the two dimensional harmonic oscillator.

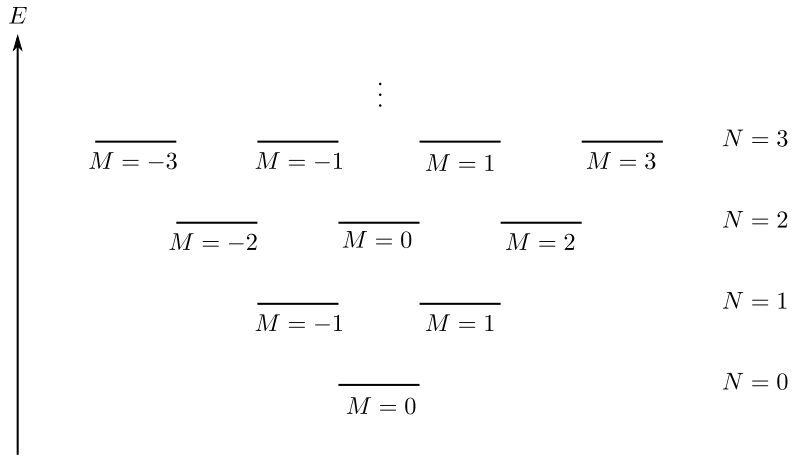

Figure 3.8: $N+1$-fold degeneracy of angular momentum states.

Figure 3.9: Illustration of the probability density of finding the atom at a given position in a two-dimensional harmonic potential.

3.2.3 Average energy of the atom in the donut dipole potential

In thermal equilibrium, the atom in the two-dimensional harmonic potential is not in a pure stationary state, but rather in a statistical mixture of stationary states $|\psi_{N,M}\rangle$ with weights proportional to e^{-E_N/k_BT}. The corresponding partition function takes the form

$$\begin{aligned} Z &= \sum_{N=0}^{\infty} g_N e^{-E_N/k_BT} \\ &= \sum_{N=0}^{\infty} (N+1) e^{-(N+1)\hbar\Omega_{\mathrm{rad}}/k_BT} \\ &= \sum_{N=1}^{\infty} N \left(e^{-\hbar\Omega_{\mathrm{rad}}/k_BT}\right)^N \\ &= \frac{e^{-\hbar\Omega_{\mathrm{rad}}/k_BT}}{\left(1-e^{-\hbar\Omega_{\mathrm{rad}}/k_BT}\right)^2} . \end{aligned} \tag{3.24}$$

From the latter, we can calculate the average total energy using athe well-known result of statistical mechanics

$$\begin{aligned} \langle U_{\mathrm{tot}} \rangle &= k_B T^2 \frac{\partial \ln Z}{\partial T} \\ &= \hbar\Omega_{\mathrm{rad}} \left(\frac{1+e^{-\hbar\Omega_{\mathrm{rad}}/k_BT}}{e^{-\hbar\Omega_{\mathrm{rad}}/k_BT}-1} \right) \\ &= \hbar\Omega_{\mathrm{rad}} \left(\frac{2}{e^{\hbar\Omega_{\mathrm{rad}}/k_BT}-1} + 1 \right) \\ &= \hbar\Omega_{\mathrm{rad}} \left(\langle n \rangle + 1 \right) . \end{aligned} \tag{3.25}$$

By comparing this relation with Eq. (3.18), the quantity

$$\langle n \rangle = \frac{2}{e^{\hbar\Omega_{\mathrm{rad}}/k_B T} - 1} \tag{3.26}$$

can be interpreted as the average vibrational number governed by the temperature T. According to the virial theorem, for a harmonic oscillator, the average potential energy is equal to the average kinetic energy. Thus, it is

$$\langle U_{\mathrm{pot}} \rangle = \langle E_{\mathrm{kin}} \rangle = \frac{\hbar\Omega_{\mathrm{rad}}}{2} \left(\langle n \rangle + 1 \right) . \tag{3.27}$$

3.3 Photon scattering rate in the donut beam

Suppose that the system is perfectly isolated. Then all processes are reversible and there is no information loss taking place. However, in reality, our atoms are not a perfectly isolated system. They rather couple to the environment which leads to decoherence. For qubits whose information is stored in the hyperfine states, decoherence may come from the interaction between the atoms and the trapping field itself. This mechanism leads to inelastic photon scattering which may change the atoms' internal states.

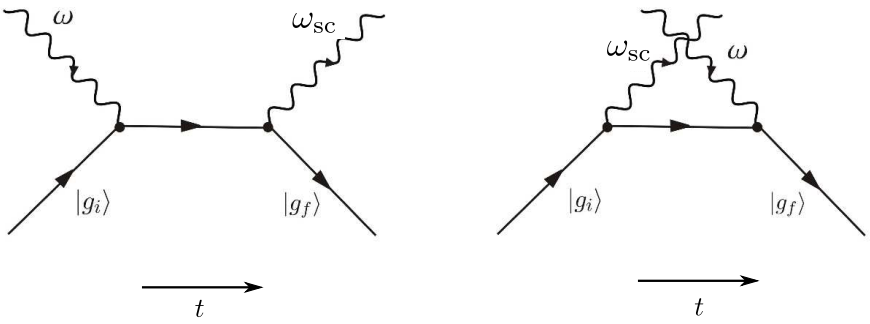

Figure 3.10: Feynman diagrams representing scattering of photons by an atom in the initial state $|g_{\mathrm{i}}\rangle$ to the final state $|g_{\mathrm{f}}\rangle$.

From the Kramer-Heisenberg formula [40], the scattering rate can be calculated using the following formula

$$\Gamma_{F,m_F \to F'',m_{F''}} = \frac{3c^2\omega^3}{4\hbar}\mathcal{I} \left| \frac{A^{(1/2)}_{F,m_F \to F'',m_{F''}}}{\Delta_{1/2}} + \frac{A^{(3/2)}_{F,m_F \to F'',m_{F''}}}{\Delta_{3/2}} \right|^2 \tag{3.28}$$

with

$$A^{(J')}_{F,m_F \to F'',m_{F''}} = \frac{\Gamma_{J'}}{\omega^3_{J'}} \sum_{q_{\mathrm{sc}},F',m_{F'}} \langle F'', m_{F''} | e\hat{\mathbf{r}} \cdot \epsilon_{q_{\mathrm{sc}}} | F', m_{F'} \rangle \langle F', m_{F'} | e\hat{\mathbf{r}} \cdot \epsilon_q | F, m_F \rangle . \tag{3.29}$$

Here $\Delta_{J'} = \omega - \omega_{J'}$ denotes the detuning of the donut laser from the ${}^6P_{J'}$ state. $\Gamma_{J'}$ and $\omega_{J'}$ are the linewidths and the resonance frequencies of the excited states. The polarizations of

the incoming and the scattered photons are indicated by q and q_{sc}, respectively. One can distinguish between two cases:

- **Rayleigh scattering**, Γ_{Ram}: In the Rayleigh scattering the atom occupies the same state before and after the scattering process. The $A^{(J')}_{F,m_F\to F'',m_{F''}}$-symbol becomes $A^{(3/2)}_{F,m_F\to F,m_F} = -A^{(1/2)}_{F,m_F\to F,m_F}$.
- **Raman scattering**, Γ_{Ray}: In the Raman scattering the state of the atom is changed after the scattering process. The $A^{(J')}_{F,m_F\to F'',m_{F''}}$-symbol reads $A^{(3/2)}_{F,m_F\to F'',m_{F''}} = 2A^{(1/2)}_{F,m_F\to F'',m_{F''}}$.

We are mainly interested in the Raman scattering since this would be responsible for the longitudinal decoherence mechanism, namely it determines the longitudinal coherence time, $T_1 = 1/\Gamma_{\mathrm{Ram}}$.

If we assume that the temperature of the atom were zero, the atom would stay at the potential minimum where it experiences zero laser intensity. This implies that the photon scattering rate would be zero. However, in reality the atom has a finite temperature so that it oscillates within the potential and sees some intensity which in turns leads to a finite scattering rate. Thus we need to know the time average intensity, $\langle\mathcal{I}\rangle$, seen by the atoms in the dipole trap. Using Eq. (3.2) and Eq. (3.27), we obtain

$$\langle\mathcal{I}\rangle = \frac{1}{\mathcal{C}}\frac{\hbar\Omega_{\mathrm{rad}}}{2}(\langle n\rangle + 1). \tag{3.30}$$

The time average photon scattering rate by an atom in the donut dipole potential can be computed by inserting Eq. (3.30) into Eq. (3.28):

$$\langle\Gamma_{\mathrm{Ram}}\rangle = \frac{3c^2\omega^3\Omega_{\mathrm{rad}}(\langle n\rangle+1)}{8\mathcal{C}}\left|\frac{A^{(1/2)}_{F,m_F\to F'',m_{F''}}}{\Delta_{1/2}} + \frac{2A^{(1/2)}_{F,m_F\to F'',m_{F''}}}{\Delta_{3/2}}\right|^2. \tag{3.31}$$

In Tabel 3.1, the calculated values of the Raman scattering rate for the two hyperfine states at different wavelengths is presented. At a high power of 1 W and small detuning, the scattering rate is less than 10 photons per second which is negligibly small. This is already expected since the atoms are trapped in the region of minimum intensity. As a comparison, the present scattering rate in the standing wave dipole trap is around 100 photons per second (see Appendix A).

Hyperfine state	Scattering rate, Γ_{sc} [s^{-1}]	λ=849.9 nm	λ=851 nm	λ=851.5 nm
$F = 3$	Raman	2.0	3.9	6.4
$F = 4$	Raman	1.9	3.7	6.1

Table 3.1: Scattering rates of the states $F = 4$ and $F = 3$ for different laser detunings at a temperature of 10 μK. The laser power $P = 1$ W and the polarization of the laser is assumed to be linear.

Therefore, the integration of the donut beam into the main experimental setup does not lead to a disturbing effect on the longitudinal coherence time T_1.

Chapter 4

Experimental realization

So far I have only discussed the generation of the donut beam (see Chapter 2) and calculated the trapping frequency depending on the laser power. From the calculations, sufficient trapping frequency needed for resolved sideband cooling in the radial direction ($\approx 2\pi \times 20\,\mathrm{kHz}$) can be implemented by extending the current experimental setup by a donut beam with a power of 1 W overlapped with the optical lattice. This amount of power can be obtained from a tapered semiconductor amplifier laser. In this chapter I will discuss the experimental setup towards integrating the donut beam into the main experiment.

4.1 Experimental setup for laser source

To save space on the main table, the laser source of the donut beam is build up on a seperated optical table.

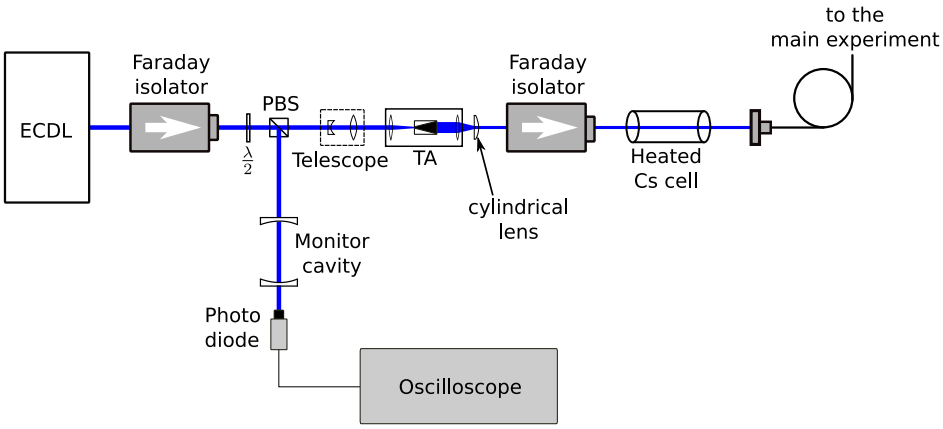

Figure 4.1: Experimental setup for high power laser.

The schematic of the setup is presented in Fig. 4.1. The laser source is a tapered amplifier (TA) diode laser seeded with an external cavity diode laser (ECDL). The output beam from the ECDL passes through a Faraday isolator and is subsequently split into two parts (monitoring and main part) using a $\lambda/2$ plate and a polarizing beam splitter (PBS). A small percentage of the monitoring part is sent through a Fabry Perot cavity for monitoring the mode of the laser while the main part is used as the seeding power for the TA diode. The

seed beam is spatially mode-matched to the beam emitted from the back facet of the TA using a telescope. Since the front output aperture of the TA is asymmetric, a cylindrical lens, in addition to a spherical lens, is used to collimate the output beam. The amplified light is again sent through another Faraday isolator. Due to the amplified spontaneous emission (ASE) of the TA diode, the output spectra can have a significant high background in the vicinity of the center wavelength which is around 850 nm. Since this wavelength region is close to the Cs resonance frequency (852 nm), light from the ASE may heat the atoms. In order to suppress the background contribution, a hole must at this resonance frequency must be burned in the laser spectrum. For this purpose the beam is sent through a heated cesium vapor cell. The heating is required to increase the cesium vapor density, and thus the absorbtion. Finally, the beam is coupled into a single mode fiber and guided to the main experiment.

The ECDL, TA diode system and the heated cesium cell have been developed during this thesis work. In the following the detailed design of each of them will be described.

External cavity diode laser

The configuration of the ECDL is illustrated in Fig. 4.2. The output from the laser diode is collimated by a lens and then incident onto a grating with 1800 lines/mm. The grating is aligned in such a way that the first order is reflected back into the laser diode, forming an external resonator together with the back facet of the diode. The zeroth diffraction order is coupled out. By adjusting the angle of the grating by means of a pizoelectric tranducer (PZT) attached to the grating's holder, the length of the resonator can be tuned, so does the output frequency which depends on the length of the resonator.

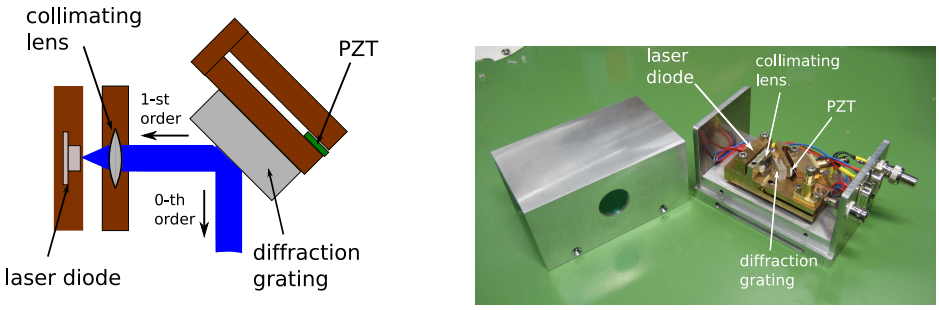

Figure 4.2: External cavity diode laser in the Littrow configuration.

TA Diode System Design

In Fig. 4.3(a) a schematic layout of a typical semiconductor laser amplifier is shown, which has a laterally tapered gain region. This tapered gain region allows for a weak signal to be injected into the narrow end and the amplified light to come out from the broad end after passing through the gain region. Both ends are anti-reflection coated in order to avoid laser action of the amplifier chip itself. A detailed review on tapered semiconductor-laser amplifiers can be found in [41]. The TA is attached to a C-mount package which acts as a heat sink (see Fig. 4.3(b)).

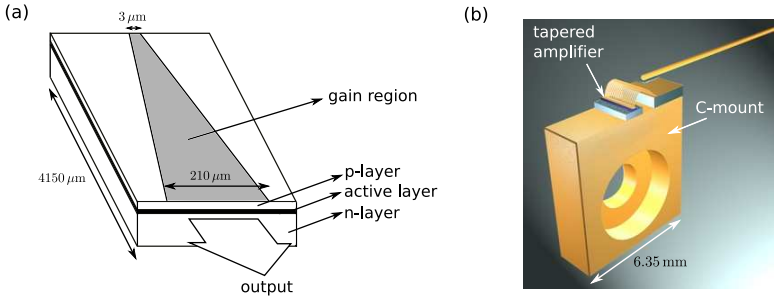

Figure 4.3: (a) Schematic layout of a tapered semiconductor laser amplifier. (b) Tapered amplifier attached onto a C-mount package [42].

In Fig. 4.4, the design of the tapered amplifier system is illustrated. It consists of a TA diode[1], two collimation lenses[2] threaded into a homemade brass tube. According to the manufacturer's datasheet, the maximum output power is about 1 W, with a center wavelength around 850 nm. The C-Mount TA diode is screwed onto a homemade brass diode holder. The tube and the holder have been precisely designed by the mechanical workshop so that the axes of the lenses coincide with the input and output aperture of the TA diode. This ensures a good coupling of the input light and collimation of the output light.

Thermal variations can cause the output power of the TA to fluctuate. For this reason, the TA system needs to be temperature stabilized. To thermally control this system, the brass holder is mount onto an aluminum plate with two peltier coolers underneath. For better heat dissipation, a water cooling system is employed. In addition, the TA system is covered with a metal housing to minimize any thermal variations caused by air movement and temperature gradient of the surrounding.

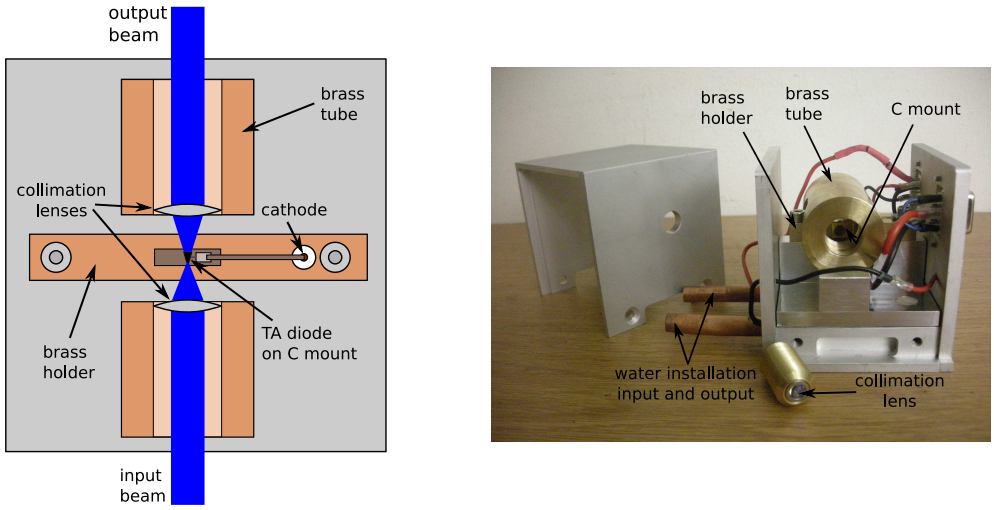

Figure 4.4: Design of the tapered amplifier system.

[1]Eagleyard Photonics, EYP-TPA-0850-01000-4006-CMT04-0000

[2]input facet: $f = 4.5$ mm 0.55 NA, Thorlabs C230TME-B; output facet: $f = 3.1$ mm 0.68 NA, Thorlabs C330TME-B

Heated cesium vapor cell

In Fig. 4.5, the design of the heated cesium cell is shown. A cesium vapor cell of 10 cm in length is put into a metal tube to ensure a homogenous temperature distribution when being heated. In order to avoid air turbulance which might be caused by high temperature gradient, metal rods with a smaller diameter are attached at both ends of the metal tube, preventing the incoming and outgoing beam from pointing instability. A heating tape is wrapped around the metal tube to heat the cesium vapor cell. To monitor the temperature, a themocouple sensor is attached at two different positions on the metal tube.

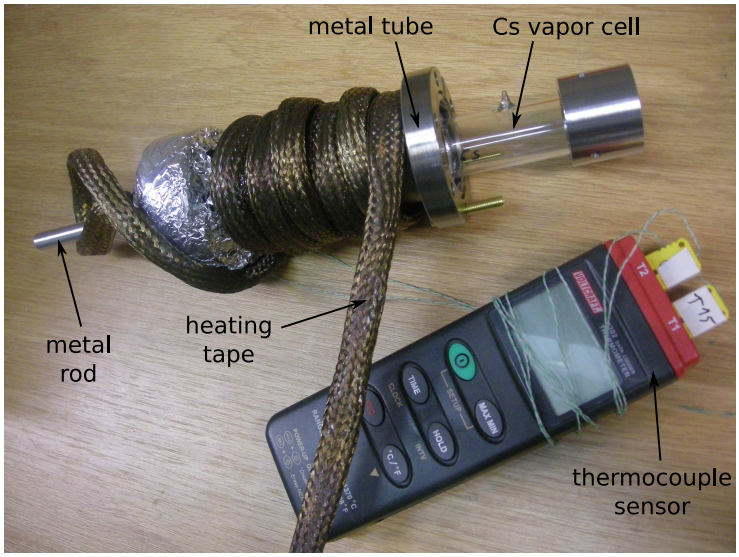

Figure 4.5: Heated cesium vapor cell.

4.2 Integration of the donut beam into the main setup

In order to include the donut beam into the existing main experimental setup, light from the experimental setup discussed in the previous section is guided to the vicinity of the main experimental setup via a single mode fiber. The output beam is passed through a SPP to generate a donut beam. The donut beam is overlapped with the existing standing wave optical lattice and coupled out from it using custom made dichrotic mirrors provided by the company Laser Component. This setup is illustrated in Fig. 4.7. The transmittivity and the reflectivity of the dichrotic mirrors provided by the company is shown in Fig. 4.6.

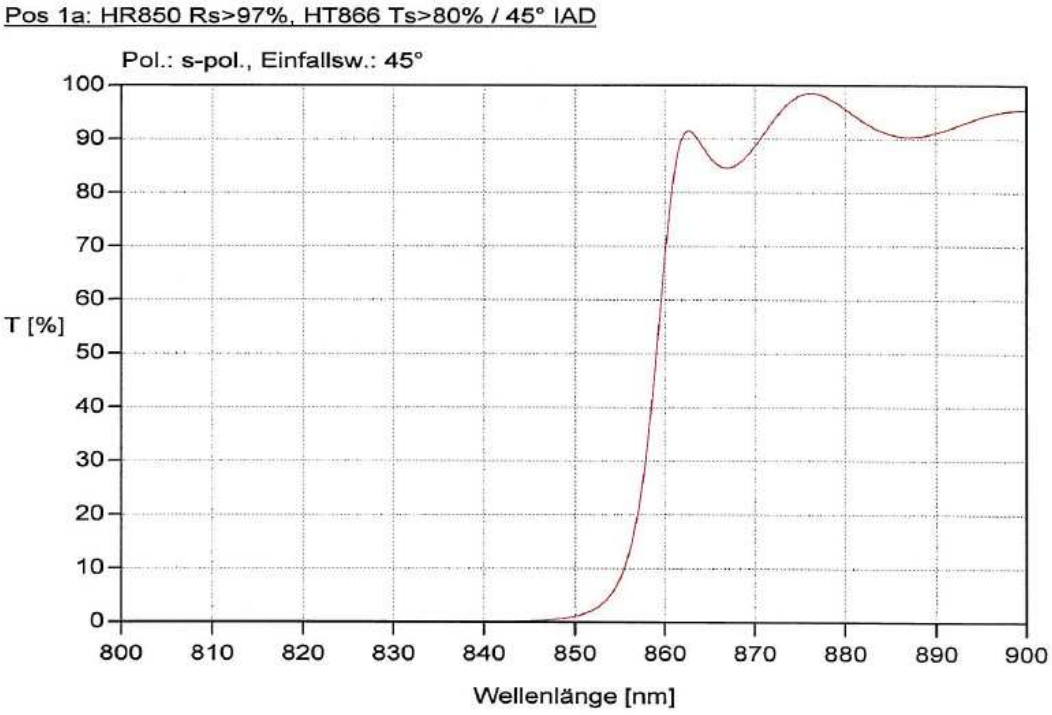

Figure 4.6: Specification of the transmittivity of the custom made dichrotic mirrors provided by the company.

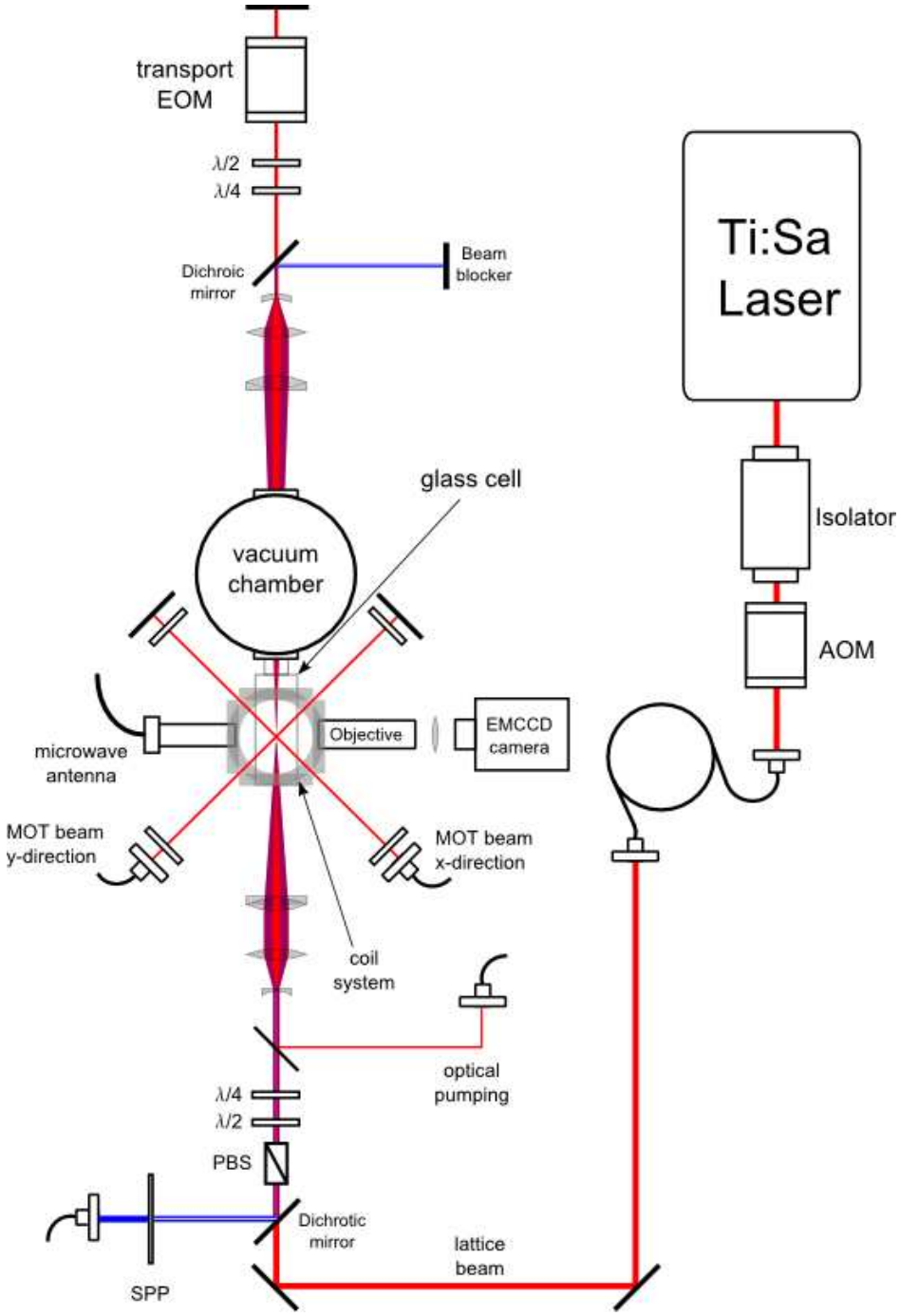

Figure 4.7: Full experimental setup. The donut beam is overlapped with the existing standing wave optical lattice and coupled out from it using dichrotic mirrors.

Chapter 5

Conclusion and outlook

In this project, a laser beam having a center dark region or a donut beam at a wavelength of 849.9 nm has been generated using a SPP. An analytical expression describing the intensity distribution of the generated donut beam after passing through an optical system that can be described by a ray transfer matirx has been derived using scalar diffraction theory. This expression can be used for any optical system, one just has to know to corresponding ray transfer matrix of the system. The range of wavelengths in which the SPP can generate a sufficiently good donut beam has also been investigated. It turns out that in the range of our interest, which is between 840 nm to 852 nm, a sufficiently good donut beam can still be generated.

Since the generated donut beam is blue-detuned with respect to the D_2-transtion, it can act as a dipole potential for Cs atoms, where the atoms can be trapped in its the center dark region. When overlapped with the existing optical lattice, it can provide a tighter confinement in the radial direction which then increase the oscillation frequency in this direction. From the calculation, by using a 1W laser, which can be obtained from a tapered amplifier laser, the oscillation frequency in the radial direction can be increased from $2\pi \times 1.1$ kHz to around $2\pi \times 20$ kHz. This offers a good condition for resolved Raman sideband cooling which can be used to cool our atoms to the motional ground state in radial direction. Once the atoms are cooled to the motional ground state in all three dimensions, atom-atom entanglement via controlled cold collisions can be demonstrated.

Appendix A

Cs atoms in a standing wave dipole trap

The following values are the parameters of Cs atoms in the current setup of the standing wave dipole trap formed by laser beams with $\lambda = 865.9\,\mathrm{nm}$, $P = 120\,\mathrm{mW}$ and $w_0 = 20\,\mu\mathrm{m}$.

Temperature	T	$10\mu\mathrm{K}$
Axial oscillation frequency	Ω_{axial}	$2\pi \times 115\,\mathrm{kHz}$
Radial oscillation frequency	Ω_{radial}	$2\pi \times 1.1\,\mathrm{kHz}$
Raman scattering rate	Γ_{Ram}	$100\,\mathrm{s}^{-2}$
Longitudinal coherence time	T_1	$10\,\mathrm{ms}$
Mean axial vibrational quantum number	$\langle n \rangle_{\mathrm{axial}}$	1.2
Mean radial vibrational quantum number	$\langle n \rangle_{\mathrm{radial}}$	200

Appendix B

Solution to the Collins integral

In this appendix, an analytical expression describing the field amplitude of a donut beam with topological charge l generated by a SPP, after propagating through an optical system, is derived.

The Collins integral

$$\begin{aligned} E(\rho,\phi,z) = &-\frac{i}{\lambda B}e^{ikz} \\ &\times \int_0^\infty E(\rho',\phi',z')\exp\left[\frac{ik}{2B}(A\rho'^2+D\rho^2)\right] \\ &\times \int_0^{2\pi}\exp\left[\frac{-ik\rho\rho'\cos(\phi-\phi')}{B}\right]\rho' d\rho' d\phi'. \end{aligned} \tag{B.1}$$

can be used to propagate an initial field at point (ρ',ϕ',z) to a final point (ρ,ϕ,z) through an optical system whose ray transfer matrix is given by

$$M = \begin{pmatrix} A & B \\ C & D \end{pmatrix}. \tag{B.2}$$

In our case, the initial field is the field amplitude immediately behind the SPP which is given by the field amplitude of the incident Gaussian beam times the phase factor introduced by the SPP

$$E(\rho',\phi',z') = E_0\frac{w_0}{w(z')}\exp\left(\frac{-\rho'^2}{w^2(z')}\right)\exp\left(-ikz'-ik\frac{\rho'^2}{2R(z')}+i\zeta(z')\right)\exp(il\phi')\,. \tag{B.3}$$

Inserting Eq. (B.3) into Eq. (B.1) we obtain

$$\begin{aligned} E(\rho,\phi,z) = &-i\frac{1}{\lambda B}E_0\frac{w_0}{w(z')}e^{ikz}e^{i\frac{kD\rho^2}{2B}}e^{-ikz'}e^{i\zeta(z')} \\ &\times \int_0^\infty \exp\left(-\frac{\rho'^2}{w^2(z')}\right)\exp\left(-i\frac{k\rho'^2}{2R(z')}\right)\exp\left(i\frac{kA\rho'^2}{2B}\right)\rho' d\rho' \\ &\times \int_0^{2\pi}\exp\left[\frac{-ik\rho\rho'\cos(\phi'-\phi)}{B}\right]\exp(il\phi')d\phi' \end{aligned} \tag{B.4}$$

The integration over the azimuthal angles gives rise to an n-th order Bessel function:

$$\begin{aligned} E(\rho,\phi,z) =&(-i)^{|l|+1}\frac{1}{\lambda B}E_0\frac{w_0}{w(z')}(2\pi)e^{ikz}e^{i\frac{kD\rho^2}{2B}}e^{-ikz'}e^{i\zeta(z')}e^{il\phi} \\ &\times\int_0^\infty \exp\left[-\rho'^2\left(\frac{1}{w^2(z')}+\frac{ik}{2R(z')}-\frac{ikA}{2B}\right)\right]J_l\left(\frac{k\rho\rho'}{B}\right)\rho' d\rho'. \end{aligned} \tag{B.5}$$

This can be further simplified with the help of the following integral [44]

$$\int_0^\infty xe^{-\alpha x^2}J_\nu(\beta x)=\frac{\sqrt{\pi}\beta}{8\alpha^{3/2}}\exp\left(-\frac{\beta^2}{8\alpha}\right)\left[I_{\frac{1}{2}|\nu|-\frac{1}{2}}\left(\frac{\beta^2}{8\alpha}\right)-I_{\frac{1}{2}|\nu|+\frac{1}{2}}\left(\frac{\beta^2}{8\alpha}\right)\right] \tag{B.6}$$

where I_m is a modified Bessel function of the first kind and m-th order.

Finally, we obtain the following analytical expression for the field amplitude behind the optical system

$$\begin{aligned} E(\rho,\phi,z) =&(-i)^{|l|+1}\frac{1}{\lambda B}E_0\frac{w_0}{w(z')}(2\pi)\frac{\sqrt{\pi}b}{8a^{3/2}}e^{ikz}e^{i\frac{kD\rho^2}{2z}}e^{-ikz'}e^{i\zeta(z_1)}e^{il\phi} \\ &\times\exp\left(-\frac{b^2}{8a}\right)\left[I_{\frac{1}{2}|l|-\frac{1}{2}}\left(\frac{b^2}{8a}\right)-I_{\frac{1}{2}|l|+\frac{1}{2}}\left(\frac{b^2}{8a}\right)\right]. \end{aligned} \tag{B.7}$$

where

$$\begin{aligned} a&=\left(\frac{1}{w^2(z')}+\frac{ik}{2R(z_1)}-\frac{iAk}{2B}\right) \\ b&=\frac{k\rho}{B}. \end{aligned} \tag{B.8}$$

Bibliography

[1] For example the group of Antony Zeilinger at the University of Vienna.

[2] P. Benioff, *The Computer as a Physical System: A Microscopic Quantum Mechanical Hamiltonian Model of Computers as Represented by Turing Machines*, J. Stat. Phys. 22, 563 (1980).

[3] R. Feynman, *Simulating Physics with Computers*, Int. J. Theor. Phys. 21, 467 (1982).

[4] Deutsch, *Quantum Theory, the Church-Turing Principle and the Universal Quantum Computer*, Proc. R. Soc. Lond. A 400, 97-117 (1985).

[5] C. Bennett and G. Brassard in Proceedings og the IEEE International Conference on Computers, Systems and Signal processing, Bangalore, India, p. 175 (1984).

[6] J. I. Cirac and P. Zoller, *Quantum Computation with Cold Trapped Ions*, Phys. Rev. Lett. 74, 4091-4094 (1995).

[7] T. Pellizzari, S. A. Gardiner, J. I. Cirac, and P. Zoller, *Decoherence, Continuous Observation, and Quantum Computing: A Cavity QED Model*, Phys. Rev. Lett. 75, 3788-3791 (1995)

[8] I. L. Chuang, *Quantum Computation with Nuclear Magnetic Resonance, in Introduction to Quantum Computation and Information*, H. K. Lo et al, editors, 311-339, World Scientific, Singapore (1998).

[9] B. Rosen, *Superconducting Circuit Implementation of Qubits and Quantum Computer Logic*, preprint (1997).

[10] G. K. Brennen, C. M. Caves, P. S. Jessen, and I. H. Deutsch, *Quantum Logic Gates in Optical Lattices*, Phys. Rev. Lett. 82, 1060-1063 (1999).

[11] D. P. DiVincenzo, "*The Physical Implementation of Quantum Computation*", 2000.

[12] A. Barenco, C. H. Bennett, R. Cleve, D. P. DiVincenzo, N. Margolus, P. Shor, T. Sleator, J. A. Smolin, and H. Weinfurter, *Elementary gates for quantum computation*, Phys. Rev. A 52, 3457 (1995).

[13] D. Jaksch, H.-J. Briegel, J. I. Cirac, C. W. Gardiner, and P. Zoller. *Entanglement of Atoms via Cold Controlled Collisions*, Phys. Rev. Lett., 82, 1975 (1999).

[14] Z. Zhang, G. Chen, *Mathematical Formulations of Atom Trap Quantum Gates*, Advances in Quantum Computation: Representation Theory, Quantum Field Theory, Category Theory, Mathematical Physics, University of Texas at Tyler (2007).

[15] O. Mandel, M. Greiner, A. Widera, T. Rom, T. W. Hänsch, and I. Bloch,*Coherent Transport of Neutral Atoms in Spin-Dependent Optical Lattice Potentials*, Phys. Rev. Lett. 91, 010407 (2003).

[16] O. Mandel, M. Greiner, A. Widera, T. Rom, T. W. Hänsch, and I. Bloch, *Controlled collisions for multi-particle entanglement of optically trapped atoms*, Nature 425, 937940 (2003).

[17] A. Härter, *Ein Aufbau zur kohärenten Manipulation und zum zustandsabhängigen Transport einzelner Atome*, Diplomarbeit, Universität Bonn (2007).

[18] M. Greiner, O. Mandel, T. Esslinger, T. W. Hänsch, and I. Bloch, *Quantum phase transition from a superfluid to a Mott insulator in a gas of ultracold atoms*, Nature 415, 3944 (2002).

[19] L. Förster, M. Karski, J. M. Choi, A. Steffen, W. Alt, D. Meschede, A. Widera, E. Montano, J. H. Lee, W. Rakreungdet, P. S. Jessen, *Microwave Control of Atomic Motion in Optical Lattices*, Phys. Rev. Lett.103, 233001 (2009).

[20] F. Grenz, *Ein System zur entarteten Raman-Seitenbandkhlung einzelner Cäsium-Atome* , Diplomarbeit, Universität Bonn (2008).

[21] N. Davidson, H. J. Lee, M. K., and S. Chu , *Raman cooling of atoms in two and three dimensions*, Phys. Rev. Lett. 72, 3158 (1993); S. E. Hamann, D. L. Haycock, G. Klose, P. H. Pax, I. H. Deutsch, P. S. Jessen, *Resolved-Sideband Raman Cooling to the Ground State of an Optical Lattice*, Phys. Rev. Lett. 80, 4149 (1997).

[22] F. Diedrich, J. C. Bergquist, Wayne M. Itano, and D. J. Wineland, *Laser cooling to the zero point energy of motion*, Phys. Rev. Lett. 62, 403406 (1989).

[23] B. E. King, C. S. Wood, C. J. Myatt, Q. A. Turchette, D. Leibfried, W. M. Itano, C. Monroe, and D. J. Wineland*Cooling the Collective Motion of Trapped Ions to Initialize a Quantum Register*, Phys. Rev. Lett. 81, 1525 - 1528 (1998).

[24] L. Allen, M.W. Beijersbergen, R.J.C. Spreeuw, J.P. Woerdman, *Orbital angular momentum of light and the transformation of LaguerreGaussian laser modes*, Phys. Rev. A 45 (1992) 81858189.

[25] M. Padgett, J. Arlt, and N. Simpson, *An experiment to observe the intensity and phase structure of Laguerre-Gaussian laser modes*, Am. J. Phys. 64 (1) (1996).

[26] N. R. Heckenberg, R. McDuff, C. P. Smith, and A. G. White, *Generation of optical phase singularities by computer-generated holograms*, Opt. Lett. 17, 221-223 (1992).

[27] N. R. Heckenberg, R. McDuff, C. P. Smith, H. Rubinsztein-Dunlop and M. J. Wegener, *Laser beams with phase singularities*, Opt. Quantum Electron. 24, S951S962 (1992).

[28] M.W. Beijersbergen, et. al., *Helical-wavefront laser beams produced with a spiral phaseplate*, Optics Communications 112, 321-327(1994).

[29] A. Muthukrishnan and C. R. Stroud, Jr.*Entanglement of internal and external angular momenta of a single atom*, J. Opt. B: Quantum Semiclass. Opt. 4, S73-S77 (2002)

[30] M. Born, E. Wolf, *Principles of Optics*, (Pergamon, New York, 1959).

[31] D. Meschede, *Optics, Light and Lasers*, Wileys, 2. Edition (2007).

[32] Stuart A. Collins, Jr., *Lens-System Diffraction Integral Written in Terms of Matrix Optics*, J. Opt. Soc. Am. 60, 1168-1177 (1970).

[33] L. Förster, *Microwave control of atomic motion in a 1D optical lattice*, PhD thesis, Universität Bonn (2010).

[34] V. V. Kotlyar, A. A. Almazov, S. N. Khonina, V. A. Soifer, H. Elfstrom, and J. Turunen, *Generation of phase singularity through diffracting a plane or Gaussian beam by a spiral phase plate*, J. Opt. Soc. Am. A 22, 849-861 (2005).

[35] Hipolito Garcia-Gracia and Julio C. Gutirrez-Vega, *Diffraction of plane waves by finite-radius spiral phase plates of integer and fractional topological charge*, J. Opt. Soc. Am. A 26, 794-803 (2009).

[36] M V Berry, *Optical vortices evolving from helicoidal integer and fractional phase steps*, J. Opt. A: Pure Appl. Opt. 6 (2004) 259268.

[37] A. Y. Bekshaev, A. I. Karamoch, *Displacements and deformations of a vortex light beam produced by the diffraction grating with embedded phase singularity* , Opt. Commun. 281, 3597 (2008).

[38] R. Grimm, M. Weidemller und Y. B. Ovchinnikov, *Optical dipole traps for neutral atoms*, Adv. At. Mol. Opt. Phys. 42, 95 (2000).

[39] Cohen Tannoudji, *Quantum Mechanics*, Vol. 1, Wiley-Interscience,(1977).

[40] R. Loudon, *The quantum theory of light*, Oxford, New York, 2. Edition (1983).

[41] J. N. Walpole, *Semiconductor amplifiers and lasers with tapered gain regions*, Opt. Quantum Electron., Vol.28, 623-645 (1996).

[42] Data sheet from Eagleyard Photonics,

"http://www.eagleyard.com/fileadmin/downloads/daten/EYP-TPA-0850-01000-4006-CMT04-0000.pdf"

[43] M. Abramowitz and I. A. Stegun, eds., *Handbook of Mathematical Functions*, National Bureau of Standards, Gaithersburg, Maryland (1964).

[44] I. S. Gradshteyn and I. M. Ryzhik, *Table of Integrals, Series, and Products*, Academic Press, New York (1980).

Acknowledgement

During the last year I had the pleasure of studying and working with a number of wonderful people who deserve thanks for their help and support during my research. First of all I would like to thank my supervisor, Prof. D. Meschede, who has opened for me the possibility to work in this absolutely fascinating and exciting area of quantum optics and quantum information. I would like to acknowledge Prof. M. Fiebig for his very kindwillingness to be the coreferent of my master thesis.

I would like to thank the members of the team, Artur Widera, Woflgang Alt, Jai-Min Choi, Michal, Leonid, Andreas, Noomen and Kohei, for the valuable discussions we had and for sharing your knowledge with me.

I would like to acknowledge all the members of the group and the institute administrative staff for friendly atmosphere you keep in the institute, for your assistance and kindness. Thanks to my parents. Whatever success I have in my life is due to the beginnings which they gave me.

I hereby certify that the work presented here was accomplished by myself and without the use of illegitimate means or support, and that no sources and tools were used other than those cited.

Bonn, in March 2010